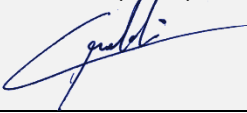# Autonomous Robotic Inspection and Maintenance on Ship Hulls and Storage Tanks

# Deliverable report – D3.3

| Context | |
|---|---|
| Deliverable title | Defect localization from a robot team |
| Lead beneficiary | CNRS |
| Author(s) | Cédric PRADALIER (CNRS), Abdelkrim Saidoum (CETIM), Naim Samet (CETIM), Quang Anh Vu (CETIM), Antoine Valentin (CETIM), Clément Jabierre (CETIM) |
| Work Package | WP3 |
| Deliverable due date | September 2023 (M45) |
| Document status | |
| Version No. | 1 |
| Type | REPORT |
| Dissemination level | PUBLIC |
| Last modified | 23 November 2024 |
| Status | RELEASED |
| Date approved | 13 December 2023 |
| Approved by Coordinator | Prof. Cédric Pradalier (CNRS) Signature: |
| Declaration | Any work or result described therein is genuinely a result of the BUGWRIGHT2 project. Any other source will be properly referenced where and when relevant. |

## Table of Contents

## LIST OF FIGURES

## LIST OF TABLES

## LIST OF EQUATIONS

## HISTORY OF CHANGES

| Date | Written by | Description of change | Approver | Version No. |
|------|-----------|----------------------|----------|-------------|
|      |           |                      |          |             |
| 12/2023 | CNRS | Proofreading | CNRS | V0.5 |
|      |           |                      |          |             |

## ABBREVIATIONS

| | |
|---|---|
| ASV | Autonomous Surface Vehicle |
| ROV | Remotely Operated Vehicle |
| AUV | Autonomous Underwater Vehicle |
| UAV | Unmanned Air Vehicle |
| QoS | Quality of Service |
| IMU | Inertial Measurement Unit |
| EKF | Extended Kalman Feature |
| UGW | Ultrasonic Guided Wave |
| LIDAR | Light Detection And Ranging |
| EMAT | Electromagnetic Acoustic Transducer |
| SAFT | Synthetic Aperture Focusing Transform |
| TFM | Total Focusing Method |
| FFT | Fast Fourier Transform |
| NeRF | Neural Radiance Fields |

## REFERENCED DOCUMENTS

- Master thesis report of Brandon Alves, within his dual master's degree at INSA Lyon and the Georgia Institute of Technology.
- D3.1 Simultaneous localisation and geometry inference on a metal plate
- D3.2 Defect localization by acoustic signal triangulation and tomography
- D6.1 Multi-crawler inspection planning and execution control
- D6.3 Multi-robot acoustic tomography planning and execution control

These documents are available on BUGWRIGHT2's Nextcloud.

# 1. Abstract

This deliverable 3.3 describes the development and evaluation of a methodology for the detection and localization of defects by a robot team. This deliverable is strongly linked to the deliverable 6.3 on multi-robot acoustic tomography planning and execution control, which is planned as a demonstration.

The work presented here follows two main development directions. A fundamental work in simulation was focused on the feasibility of defect mapping using multi-robot perception, under the specific assumption that the existence of a defect between an emitter and a receiver can be detected reliably. The second part of this work focused on an evaluation of the practical feasibility of long-distance guided wave generation from a mobile robot. The final section of this document describes the use of machine learning to detect the presence of a defect on the path of the waves.

# 2. Multi-robot defect detection

This section of deliverable D3.3 focuses on the detection of defects in a metal structure using a team of robot. A significant part of this section has been included in the Master thesis report of Brandon Alves, within his dual master's degree at INSA Lyon and the Georgia Institute of Technology.

This study is part of the broader context of the European BUGWRIGHT2 project, which aims to solve the problem of autonomous inspection and maintenance of large metal structures with heterogeneous fleets of mobile robots. In this section, we focus on the development of navigation strategies for a set of mobile robots using Ultrasonic Guided Wave (UGW), or Lamb waves, to perform the inspection of metal plates. Indeed, guided waves have the particularity of propagating along a plate by interacting with the material that composes it, and by being affected by changes in geometry related, in particular, to corrosion.

The main problem is therefore to define multi-robot navigation strategies to optimize the acquisition of data allowing to perform a tomography of metallic surfaces.

The expected contributions of this section are as follows:

- Development of multi-robot navigation strategies for the acoustic inspection of metallic structures.
- Optimization of data acquisition for performing tomography.
- Implementation of navigation methods in a simulation environment.

## 2.1.    Preliminary definitions

Here, we will explain the preliminary assumptions and definitions that will be used in the remainder of this report. First, we consider a planar environment, bounded and of known size. We assume here that each robot is able to know its position in the environment. We also assume that the obstacles are localized in the environment. Only the corrosion areas are not located.

We use robots of the type *crawlers*. These robots are equipped with two drive wheels and an castor wheel. An example of two theoretic crawlers is shown in **Figure 1**, this theoretic representation is inspired from Roboplanet's (RBP) Altiscan. The pose of the robot is defined by a triple $(x, y, \theta)$ where $x$ and $y$ are the coordinates of the robot in the environment and $\theta$ is the orientation of the robot in the environment. Because the structure surface can be assimilated to a 2D manifold embedded in 3D, we assume a 2D

representation of the problem is sufficient. We assume that the pose of the robot is known. We also assume that the robots are able to synchronize in order to be able to move simultaneously or alternatively. We note $cr$ the unit cost of rotation of the robot and $ct$ the unit cost of translation of the robot.

Each robot is either a transmitter or a receiver, or both. Crawlers are equipped with different sensors. Among them:

- an IMU (Inertial Measurement Unit) sensor
- a UGW (Ultrasonic Guided Waves) sensor
- a LIDAR (Light Detection And Ranging) sensor
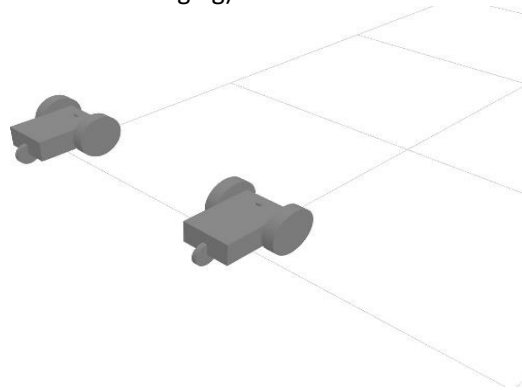


Figure 1: Crawler model used for acoustic inspection of metal structures

The IMU sensor makes it possible to know the orientation of the robot in the environment. The UGW sensor detects the presence of corrosion on the metal surface by emitting and receiving ultrasonic waves. The LIDAR sensor detects obstacles in the environment. The obstacles considered here are mainly the other robots inspecting the metal surface. Corrosion zones are detected by the emission of ultrasonic waves by a robot and the reception of these waves by another robot. In this section, we assume that as long as the wave received by one of the crawlers is altered, then there is a point of corrosion between the transmitter robot and the receiver robot. However, the position and extent of the defect on this segment is not observable. The detection of these corrosion zones is carried out in real time. The maximum range of ultrasonic waves is noted $d_{max}$. The wave propagation being very fast in metal plate (approx. 5000m/s) in comparison to the robot displacement, we assume an instantaneous transmission of the wave between the emitter and the receiver.

We use an occupancy grid to model the environment in which robots evolve during the acoustic inspection of metal structures. This grid allows us to represent and categorize the different states of the areas of the metal surface. The occupancy grid is composed of cells, where each cell corresponds to a small region of the environment. In particular, we used a resolution of 0.05 meters per cell. We use three states to characterize these cells: unknown, empty and occupied. Unknown status refers to areas whose status has not yet been determined or detected. The empty state indicates areas where there is no corrosion detected, i.e. the metal surface is sound. Finally, the occupied state represents the identified corrosion areas, where the presence of defects or deterioration is detected.

By using this occupancy grid, we can track and update in real time the status of different areas of the metal surface during the inspection. This allows us to plan robot movements, optimize their trajectory and ensure full coverage of the surface to be inspected. In addition, this representation gives us a clear view of the state

of corrosion of the metal structure, thus facilitating the analysis and evaluation of the results of the inspection.

In the rest of this section, we will detail the algorithms and methods used to update the occupancy grid according to the information collected by the robots' sensors. In deliverable D6.3, we will also discuss multi-robot navigation strategies that leverage this modelling to optimize data acquisition and improve the efficiency of acoustic inspection.

## 2.2.    Background

We present here the state of the art in the field of multi-robot navigation and control for the acoustic inspection of metal structures. The objective of this literature review was to collect key information, analyse previous work and situate our project in the existing research context. The references and sources cited in this section provide a solid foundation of knowledge and expertise on the subject.

Initially, we were interested in the properties of ultrasonic guided waves and their applications in the field of tomography [1] and [2], mapping of robots and metallic structures [3], [4], [5], robots and sensors used in our project [6], multi-robot exploration [7], [8] as well as placement strategies for detection [9], [10], [11].

In [1] and in deliverable D3.1 (Simultaneous localisation and geometry inference on a metal plate), we proposed a method to infer the geometry of metal plates using Lamb waves. We used beamforming [12] to estimate plate boundaries based on acoustic measurements in a pulse-echo context. Experimental results show accurate inference of plate geometry. However, this work was only considering the mapping of the contours of the structures, without proposing a method to map the defects, which is the subject of our problem.

In [3], the authors present a FastSLAM-based approach [13] for robotic inspection of metal structures using ultrasound. They propose a pioneer edge allocation method for multi-robot exploration, allowing fast and accurate inspection of structures. Our work takes robot localization and mapping as known and focuses multi-robot mapping (this deliverable) and on trajectory planning for the inspection of metal structures (D6.3). The approach used in this article can therefore be complementary to our work.

In the paper [14], the authors propose a method for mapping metallic structures using UGW waves. They combine a Cartesian grid with specific features for fault detection. The experimental results show an accurate mapping of metallic structures. However, the authors are once again content to map the outlines of the structures, without proposing a method for mapping the defects.

The article [4] focuses on the localization of impacts in composite structures using a complex imaging method. The authors use piezoelectric sensors [15] to detect and localize impacts, and a wavelet transform method [16] to analyse acoustic signals. Experimental results show accurate detection and localization of impacts. The sensors used are similar to those used in our project, but these sensors are positioned in a fixed way on the structure, while we want a mobile strategy.

The paper [2], the authors propose a high-resolution ultrasound tomography method for the quantification of wall thickness. They exploit the dispersive nature of Lamb waves to convert variations in thickness into variations in wave velocity, thus enabling accurate reconstruction of wall thickness. Experimental results show accurate reconstructions of corrosion defects. This article was interesting to understand the properties of guided ultra- sonic waves and their applications in the field of tomography.

The article [6], resulting from the work of BUGWRIGHT2, presents a magnetic robot system for the inspection and autonomous maintenance of large structures. The authors propose a localization framework based on a grid created from a point cloud, coupled with ultra-wideband (UWB) sensors and an inertial measurement unit (IMU). They also incorporate a piezoelectric sensor for UGW wave detection for precise robot localization and structural feature mapping. It is typically these robots and sensors that are used in our work.

The paper [7] presents a planning algorithm for multi-robot exploration. This algorithm, called *MinPos*, is designed to efficiently allocate boundaries to robots in order to minimize the movement and time needed to explore the environment. It uses advanced optimization techniques to solve this problem effectively. However, our work focuses on structural inspection for flaw detection. We want a detailed inspection of corrosion areas and not a global exploration of the environment.

The article [9] presents strategies for the optimal placement of surveillance cameras in art galleries. The authors propose methods to maximize surveillance coverage while minimizing the number of cameras needed. However, the sensors used in our project are sensors that provide information on a segment only, between a transmitter and a receiver, and not global information like a camera. The sensors used in our project are shown in section section 2.1.

In the article [8], the authors propose a method for automatically locating and sizing defects in structures using guided wave imaging. They use a convolutional neural network [17] to analyse guided wave signals and estimate defect sizes. The experimental results show the efficiency of the proposed approach to invert both synthetic and experimental data. This approach requires fixed sensors on the structure. We want to study a mobile approach, not requiring the deployment of sensors on the structure.

The article [5] presents an autonomous on-plate exploration for an inspection robot using UGW waves. The authors propose a localization method based on a mesh created from a cloud of points and use measurements from IMU and UWB sensors. They also integrate a piezoelectric sensor into the system for precise robot location and structural feature mapping. In our approach, the location is assumed to be known. This work can be used for robot localization, although this is not the subject of our project. Nevertheless, the type of robot and sensors used are similar to those used in our project.

The article [10] presents effective measurement planning strategies for remote gas detection with mobile robots. The objective of the study is to optimize the planning of measurements so as to maximize gas detection accuracy while minimizing the time and resources required. The authors propose different approaches for planning measurements, including the use of exploration techniques based on the boundaries of detection zones, the selection of efficient trajectories to cover the environment and the reduction of the number of measurements necessary by using probabilistic models. The type of sensor used has characteristics similar to those of the sensors used in our project. However, our problem imposes movements of pairs of robots. The way to split the investigation into two phases, a rough inspection phase and a refinement phase, is also similar to our approach presented in D6.3. However, this first phase is performed by fixed sensors, which is not desirable in our approach. We will also use a TSP (Traveling Salesman Problem) to optimize robot movements between areas of interest.

In the paper [11], the authors propose an efficient measurement planning method for remote gas detection with mobile robots. Their approach is to optimize the planning of measures in order to minimize the time

and resources required. To do this, they use a convex relaxation technique in order to solve the optimization problem which allows to minimize the number of necessary measurements, while guaranteeing a complete coverage of the environment. This study is interesting for our problem and could inspire improvements of our approach in the optimization of the TSP used.

In summary, the works presented in this section are interesting for our problem, because they allowed us to deepen our knowledge of the problems related to guided wave tomography. The articles [11] and [10] are the closest to our problem. However, these articles focus on covering the environment without worrying about the quality of the mapping of the areas of interest. Moreover, these items use fixed sensors on the structure for the first rough inspection phase, which is not desirable in our approach. This is why we propose a multi-robot navigation approach for the acoustic inspection of metallic structures in order to optimize the acquisition of data which will allow to carry out the tomography of metallic surfaces.

## 2.3.    Methodology

We have developed three specific strategies to optimize data acquisition and enable the tomography of metallic surfaces. These three strategies are:

1. *Roller Painting* navigation strategy
2. *Nordic Skiing* navigation strategy
3. *Polygonal Investigation* navigation strategy

Among these strategies, the first two are non-reactive and can be considered as coarse exploration strategies with the objective of quickly obtaining a global coverage of the surface to be inspected. The third strategy is reactive and makes it possible to optimize the acquisition of data for the realization of the tomography. These three strategies aim to map the metal surface and detect areas of corrosion. We will define and evaluate these three navigation strategies in deliverable D6.3 (Multi-robot acoustic tomography planning and execution control). We quickly present the roller painting and polygonal investigation strategies here, so as to explain our mapping strategies. We explain here how the data structure used for mapping corrosion areas, an occupancy grid, is updated based on information collected by the robots' UGW sensors.

### 2.3.1.    Occupancy grid update process for mapping

When scanning the surface to be inspected by a pair of transmitter and receiver robots, the transmitter robot emits an acoustic wave in the metal structure, which is then received by the receiver robot. The detection being considered as perfect, the receiver robot receives the wave emitted by the transmitter robot, without significant alteration of the power of the signal, if and only if the line segment between the two robots does not cross a zone of corrosion. It is thus possible to determine whether a corrosion zone is present between the two robots by checking how the signal received by the receiving robot is modified. We will report experiments evaluating the feasibility of this detection in practice at the end of this deliverable. Insofar as there is no detection of corrosion between the transmitter and the receiver, then the line segment between the two robots is considered to be free of corrosion. Otherwise, then the points of the line segment between the two robots are considered to be potentially corroded, with the exception of the points previously perceived to be free of corrosion. The presence of corrosion on the segment is therefore overestimated. The displacement strategies will aim to carry out several measurements, to reduce this overestimation, and approach the real shape of the corrosion.

**Algorithm 1:** Process of updating the occupancy grid using Bresenham's line algorithm.

**Data:** $P_1 \in \mathbb{R}^2$, $P_2 \in \mathbb{R}^2$, $pw \in \mathbb{R}$, $threshold \in \mathbb{R}$, $G$:
$l \times w \to [\text{UNKNOWN}, \text{EMPTY}, \text{OCCUPIED}]$, $l \in \mathbb{N}$, $w \in \mathbb{N}$
with $P_1$ and $P_2$ the two points to connect, $pw$ the power of the UGW, $threshold$ the threshold above which the power of the UGW is considered undistributed and $G$ the grid to update.

**Result:** The updated grid.

1   $p_0 \leftarrow \text{from\_position\_to\_grid\_coordinate}(P_1)$
2   $p_1 \leftarrow \text{from\_position\_to\_grid\_coordinate}(P_2)$
3   **if** $is\_out\_of\_grid(p_0)$ **or** $is\_out\_of\_grid(p_1)$ **then**
4    | **return**
5   **end**
6   $dx \leftarrow p_1.x - p_0.x$
7   $dy \leftarrow p_1.y - p_0.y$
8   $sx \leftarrow \text{sign}(dx)$
9   $sy \leftarrow \text{sign}(dy)$
10   $err = dx - dy$
11   **while** $p_0 \neq p_1$ **do**
12     **if** $pwd \leq threshold$ **and** $G(p_0) = UNKNOWN$ **then**
13      | $G(p_0) \leftarrow \text{OCCUPIED}$
14     **end**
15     **else if** $pwd > threshold$ **then**
16      | $G(p_0) \leftarrow \text{EMPTY}$
17     **end**
18     $e2 \leftarrow 2 \times err$
19     **if** $e2 > -dy$ **then**
20       $err \leftarrow err - dy$
21       $p_0.x \leftarrow p_0.x + sx$
22     **end**
23     **if** $e2 < dx$ **then**
24       $err \leftarrow err + dx$
25       $p_0.y \leftarrow p_0.y + sy$
26     **end**
27   **end**

Figure 2: Algorithm for the update of the grid status

We now only need to determine which cells of the occupancy grid are crossed by the line segment between the two robots. We use Bresenham's line algorithm to determine the points of the line segment between the two robots. The algorithm is presented above. The part adapted to our problem is between lines 12 and 17 of the latter. At this point, we check if the signal strength is sufficiently impaired and if the point of the line segment between the two robots has not already been perceived as free of corrosion. If so, then the considered point is marked as corrosion, modelled by the value OCCUPIED. If the signal strength is not sufficiently altered, then the considered point is marked as being free of corrosion, modelled by the value EMPTY. Once all the points of the segment have been traversed, the G grid is updated with the new information. Bresenham's line algorithm thus contributes to the construction of the occupation grid which

makes it possible to locate the corrosion zones detected by the robots during the acoustic inspection of metal structures.

As the metal surface is explored, the occupation grid is updated based on the information gathered by the robots. More precisely, the cells of the occupancy grid that identify corrosion elements are updated with the occupied state, while the cells that identify healthy areas are updated with the empty state. We thus end up with an occupation grid which represents the state of corrosion of the metal surface, with, for each corrosion zone, an approximation of the convex hull of the corrosion zone.

A number of environments have been prepared in simulation to tests the defect capabilities as a function of the number of defects and their density. These environments are illustrated here:



(a) Test worlds with 5 corrosion zones.



(b) Test worlds with 8 corrosion zones.



(c) Test worlds with 11 corrosion zones.



(d) Test worlds with 15 corrosion zones.



(e) Test worlds with 20 corrosion zones.

(f) Test worlds with 30 corrosion zones.

(g) Test worlds with 11 complex corrosion areas.

(h) Test worlds with 15 complex corrosion areas.

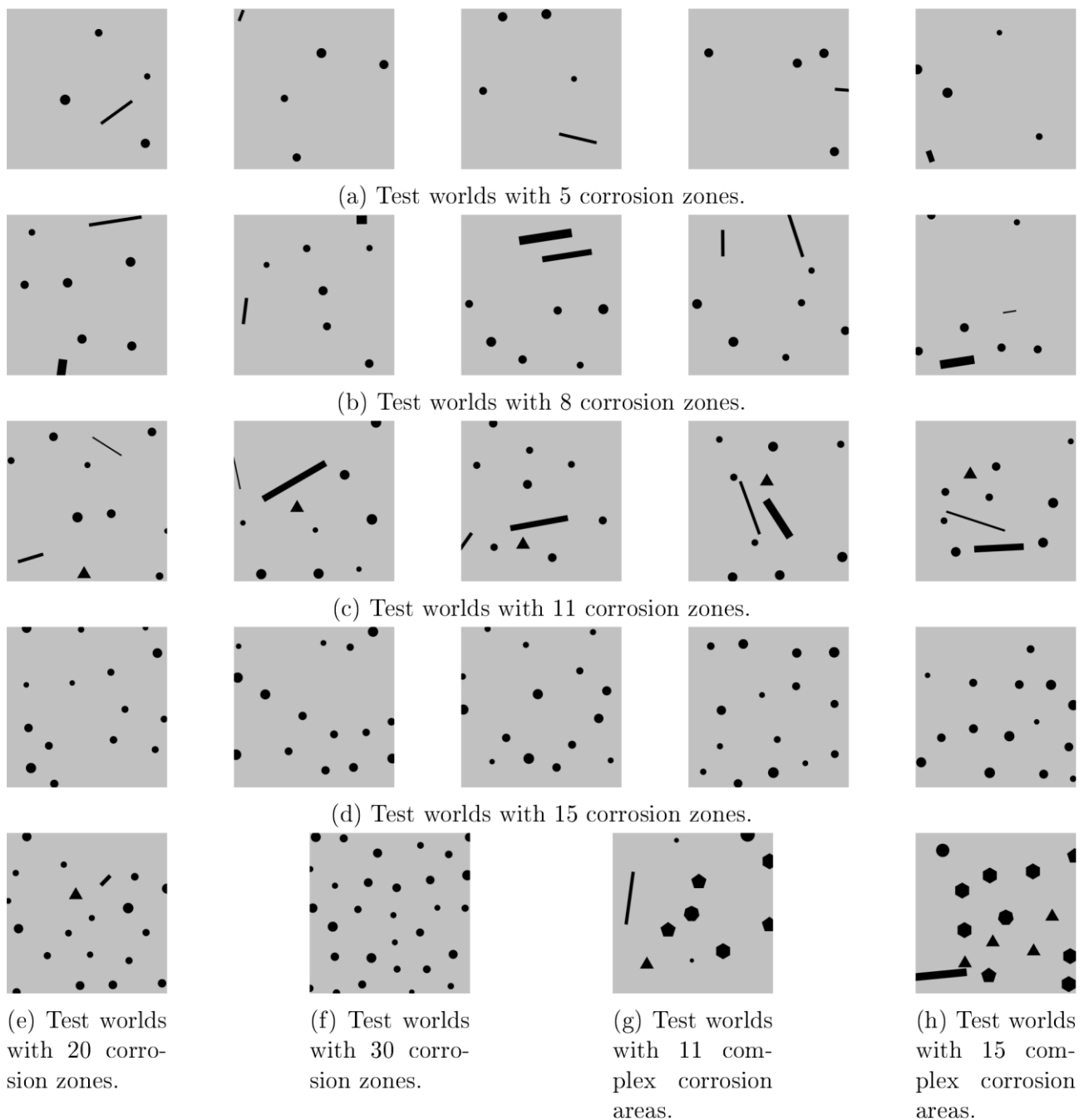Figure 3: Different test environments

## 2.3.2. *Roller Painting* navigation strategy

The first navigation strategy we propose is the *Roller Painting* navigation strategy. We chose this name for this strategy because the movement of the robots during this strategy is similar to that of a paint roller when painting a wall. This strategy is based on a rough exploration of the surface to be inspected, where the robots move in a straight line on parallel trajectories, guaranteeing global coverage of the inspection area.

The fact that the robots move along a parallel trajectory and simultaneously, implies that the rays of the signal emitted by the transmitter robot and received by the receiver robot, always have an orientation of $0$ radian for the vertical phase and an orientation of $\pi$ radians for the horizontal phase. Thus, this strategy will only be able to approach the convex hulls of the corrosion zones by rectangles.

Examples of occupancy grids resulting from the *Roller Painting* navigation strategy, represented as images, where the cells of the grid correspond to the pixels of the images, are shown below:



(a) $d = 1$ m

(b) $d = 2$ m

(c) $d = 3$ m

(d) $d = 6$ m
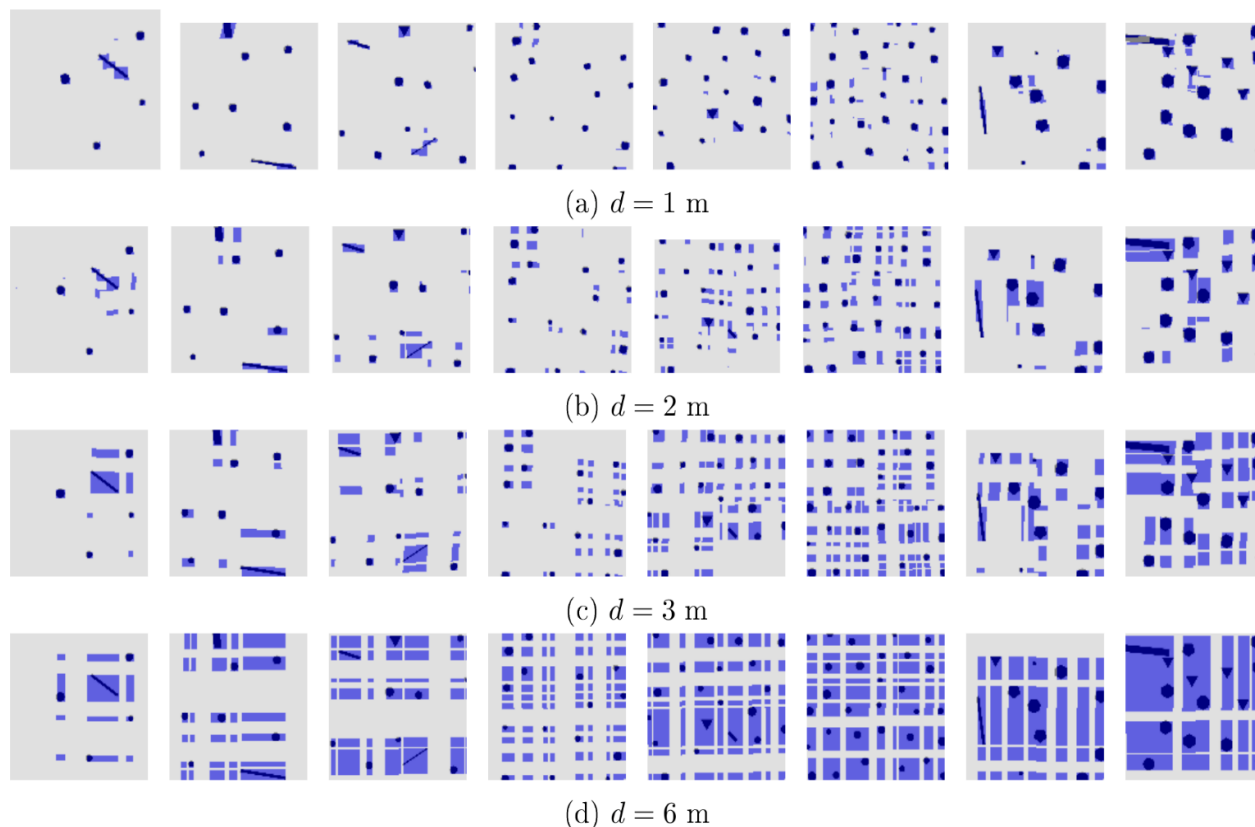
Figure 4: Overlay of the investigation maps with the mapping of the corrosion zones obtained for the different test worlds, for the *Roller Painting* method

## 2.3.3. *Polygonal Investigation* navigation strategy

The third strategy we propose is the *Polygonal Investigation* navigation strategy. We have seen, previously, that at the end of the realization of the navigation strategy *Roller Painting*, the convex hull of the corrosion zones was approximated by a rectangle. This approximation is a little more precise for the navigation strategy *Nordic Skiing*. It would be interesting to have a greater degree of precision around potential areas of corrosion. This is what we propose with the navigation strategy *Polygonal Investigation*. This strategy consists of investigating around potential areas of corrosion, previously detected by one of the two

previous navigation strategies. It consists of positioning the robots around the corrosion zones and making them move along a polygonal trajectory, so that the rays of the signal emitted and received have an orientation of greater variation even around these zones.

> **Definition 1** (Phantom zone). *A phantom zone is a corrosion zone detected by one of the navigation strategies, but which is not a corrosion zone. It is a false positive.*

The *Polygonal Investigation* navigation strategy has two advantages. The first is that it quickly eliminates phantom zones. The second is that it makes it possible to approach the convex envelopes of the corrosion zones by more diverse and precise shapes than rectangles due to the great variation in the orientation of the rays of the signal emitted and received by the robots around each vertex of the polygon.

This strategy requires two steps prior to its execution:

1. The extraction of the corrosion zones detected by one of the preceding navigation strategies.
2. Determining the order of investigation of corrosion areas.

The first step can be solved using a strongly connected component graph decomposition algorithm. The second step can be solved using a TSP (*Travelling Salesman Problem*) algorithm in the case where the number of teams $k$ is equal to 1 and a mTSP (*(multiple depot) multiple Traveling Salesman Problem*) algorithm in the case where the number of teams $k$ is strictly greater than 1. There are several solution paradigms to solve this type of problem. A first is to find an exact solution using an integer linear programming algorithm. A second is to find an approximate solution using a meta-heuristic. More details on this algorithm can be found in D6.3 (Multi-robot acoustic tomography planning and execution control) and on the thesis of Brandon Alves (see References).

## 2.3.4. Experiments

In this section, we present the experiments we conducted to validate and evaluate our different multi-robot navigation and control strategies in the context of acoustic inspection of metal structures. These experiments aim to demonstrate the efficiency, precision and reliability of our system in detecting and locating corrosion zones.

To carry out these steps, we chose to perform our experiments using *Gazebo*, a well- established simulation environment in the field of robotics. We started by building several test maps. These maps model a flat surface on which are placed simple geometric shapes, rectangles and circles, and more complex shapes, polygons between 3 and 8 vertices. These different geometric shapes represent the corrosion areas that we want to detect and locate. We presented in Figure 3 the maps we built for our experiments. Each of these subplots is sized 6 meters by 6 meters. The number of corrosion zones varies between 5, 8, 11, 15, 20 and 30 zones. The size and location of corrosion areas are randomly generated. For the maps of 5, 8, 11 and 15 zones, we generated 5 different maps in order to have more representative results. We did not generate several maps for the 20 and 30 zone maps, the polygonal investigation time being too long.

We also simulated the UGW sensor by exploiting the simulation of a UWB sensor. This UWB sensor makes it possible to emit a pulse and to receive it. By measuring the signal strength, we are able to know whether the signal has passed through an object or not. The behaviour of this UWB sensor is therefore similar to that of the UGW sensor, namely that it makes it possible to detect the presence of an object between two points, but not to locate it.

We will present the evaluation of the navigation itself in D6.3. The performance of the three navigation strategies is evaluated in terms of Cohen's $\kappa$ and inspection time. For the *Roller Painting* and *Nordic Skiing* strategy, we only used two robots. For these two strategies, we varied the distance $d$ between the robots. For the *Nordic Skiing* strategy, we also varied the pitch $s$ between the robots. For the *Polygonal Investigation* strategy, we vary the number of robots $n$, the number of teams $k$ and the number of sides $p$ of the polygons used. We use the result of the navigation strategy *Roller Painting* as a starting point. We justify this choice by the fact that this strategy is the fastest and least accurate and therefore the most likely to benefit from an improvement from the *Polygonal Investigation* strategy, without reaching inspection times too long. We therefore vary the parameter $d$ of this strategy. We summarize the experimental parameters used for each strategy in **Table 1**.

Table 1: Experimental settings used for each navigation strategy

| Strategy | Parameter | Values |
|---|---|---|
| *Roller Painting* | $n$ | 2 |
| | $d$ | 1, 2, 3, 6 (meters) |
| *Nordic Skiing* | $n$ | 2 |
| | $d$ $s$ | 1, 2, 3, 6 (meters) |
| | | 1, 2, 3, 6 (meters) |
| *Polygon Investigation* | initial strategy | *Roller Painting* |
| | $d$ $n$ $k$ $p$ | 1, 2, 3, 6 (meters) |
| | | 2, 4 |
| | | 1, 2 |
| | | 4, 6 |

During these simulations, we expect to have certain results. Among them, we expect the *Roller Painting* strategy to be the fastest, but also the least accurate. Conversely, we expect the *Polygonal Investigation* strategy to be the most accurate, but also the slowest. We also expect the $d$ parameter to have an impact on the accuracy and inspection time of the *Roller Painting* and *Nordic Skiing* strategies. A low $d$ distance should provide better accuracy but should also increase inspection time. Moreover, we expect that the $s$ parameter will also have an impact on the accuracy and inspection time of the *Nordic Skiing* strategy. A low $s$ distance should provide better accuracy but should also increase inspection time. We also expect the $p$ parameter to have an impact on the accuracy and inspection time of the *Polygonal Investigation* strategy. A low number of sides $p$ should provide better accuracy but should also increase inspection time.

Next, we expect the parameters $k$ and $n$ to have an impact on the inspection time of the *Polygonal Investigation* strategy. A high number of teams $k$ or a high number of robots $n$ should allow to obtain a lower inspection time. Finally, we expect the number of corrosion zones to have an impact on the inspection time of the *Polygonal Investigation* strategy, but not on the *Roller Painting* and *Nordic Skiing*

strategies. The higher the number of corrosion areas, the higher the inspection time should be for the *Polygonal Investigation* strategy.

Finally, we expect the number of corrosion zones to have an impact on the accuracy of the different strategies. The greater the number of corrosion areas, the lower the accuracy should be. Indeed, the higher the number of corrosion zones, the higher the probability of ghost zones appearing for the *Roller Painting* and *Nordic Skiing* strategies. For the *Polygonal Investigation* strategy, the higher the number of corrosion zones, the greater the probability that two distinct corrosion zones were confused into one during the *Roller Painting* or *Nordic Skiing* strategies.

The different results from the different simulations carried out have been presented in the preceding figures. On these images, it is possible to see in black the real areas of corrosion and in blue the areas detected as having corrosion by the various navigation algorithms.

(a) $k = 1$, $n = 2$, $p = 4$, $d = 1$ m

(e) $k = 1$, $n = 2$, $p = 6$, $d = 1$ m

(b) $k = 1$, $n = 2$, $p = 4$, $d = 2$ m

(f) $k = 1$, $n = 2$, $p = 6$, $d = 2$ m

(c) $k = 1$, $n = 2$, $p = 4$, $d = 3$ m

(g) $k = 1$, $n = 2$, $p = 6$, $d = 3$ m

(d) $k = 1$, $n = 2$, $p = 4$, $d = 6$ m
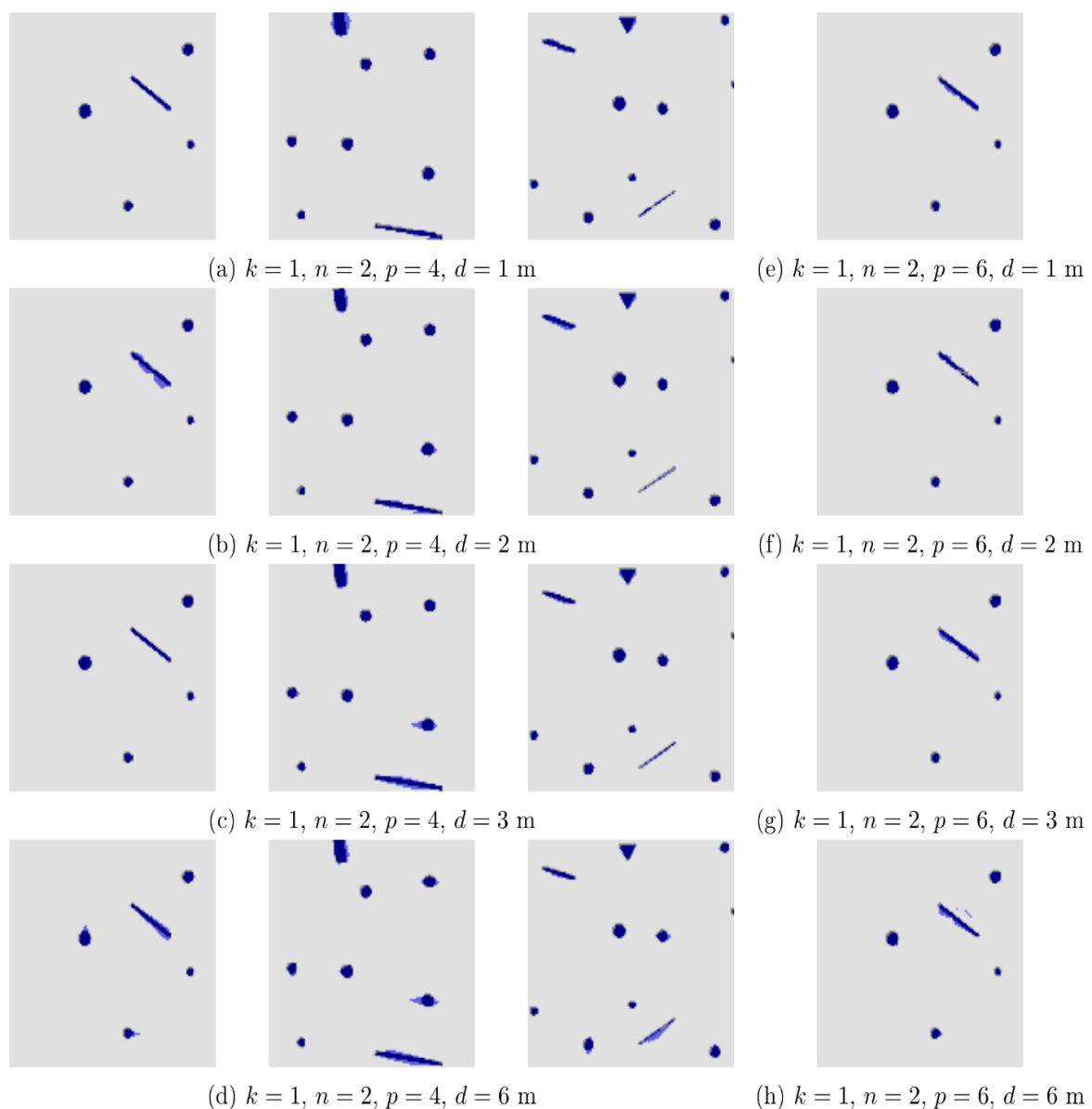
(h) $k = 1$, $n = 2$, $p = 6$, $d = 6$ m

Figure 5: Overlay of the investigation maps with the map of the corrosion zones obtained for the different test worlds, for the *Polygonal Investigation* method

## 2.4.  Results

### 2.4.1.  *Roller Painting* navigation strategy

We summarize in **Figure 6**(a) the evolution of the Cohen score as a function of the density of the world for each value of $d$. We also summarize in **Figure 6**(b) the evolution of the inspection time according to the density of the world for each value of $d$.

First, we can observe that the Cohen score generally decreases with the number of corrosion zones. There are exceptions, notably for the map composed of 15 corrosion zones, where the Cohen score is higher than for the maps composed of 5, 8 and 11 corrosion zones. This is explained by the fact that in the maps composed of 5, 8 and 11 corrosion zones, we have introduced corrosion zones with elongated shapes unlike the map composed of 15 corrosion zones where the corrosion zones are all circles. Indeed, elongated corrosion zones have a greater probability of causing phantom zones to appear, illustrated in **Figure 8** than circular corrosion zones. These phantom zones are areas free of corrosion which are detected by the crawlers. These are therefore false positives which reduce the Cohen score. These phantom zones are also more likely to appear when the density of the world is high and therefore the corrosion zones are closer to each other, or when the distance $d$ between the two crawlers is high. This is what we can observe in **Figure 7**(a) where the Cohen score decreases when the distance $d$ between the two crawlers increases. We observe that there seems to be a linear relationship between the Cohen score and the distance $d$ between the two crawlers.
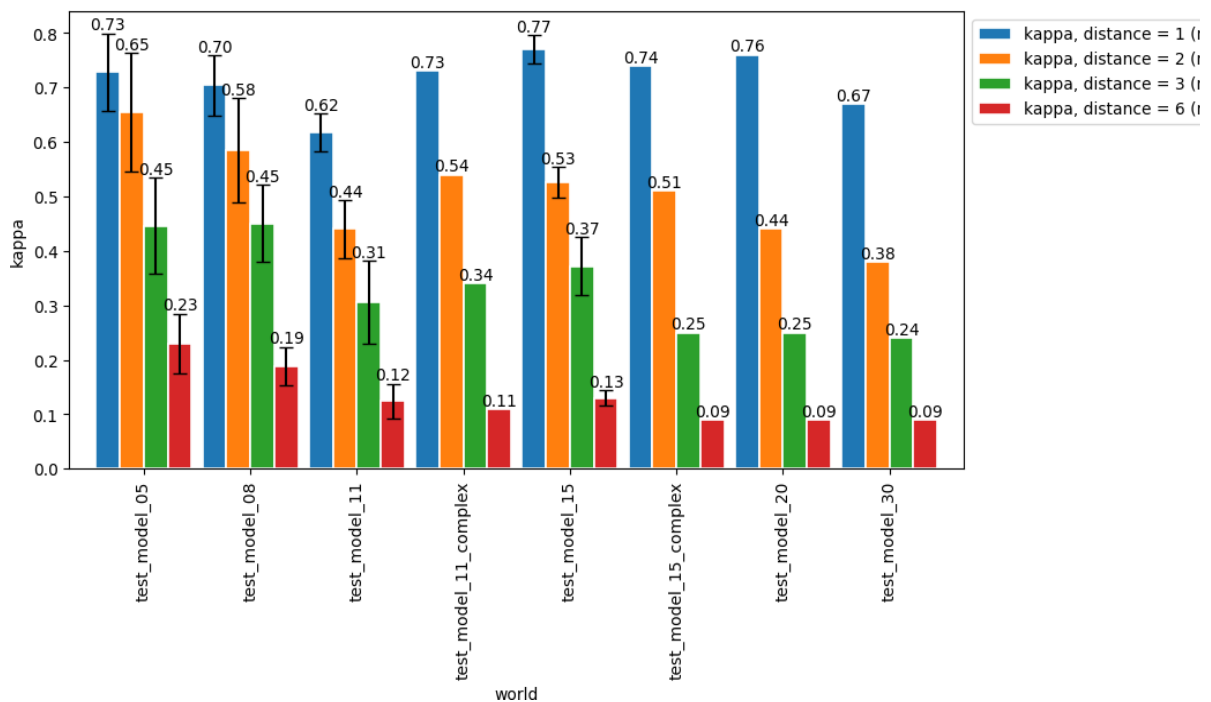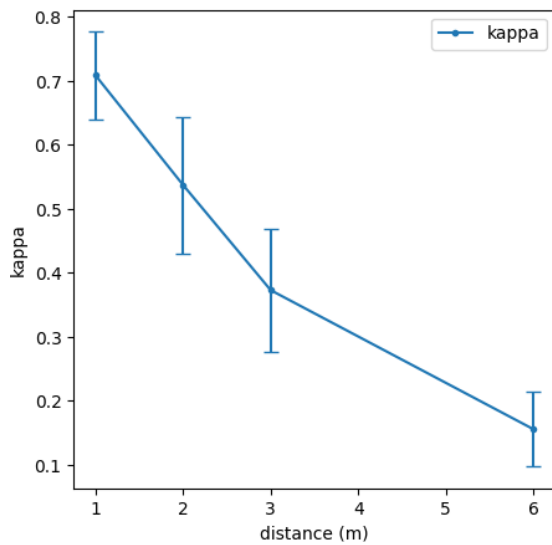


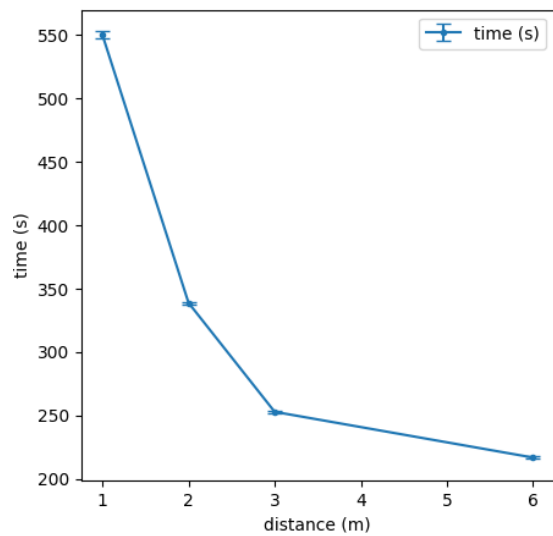(a) $\kappa$ according to the density of the world.
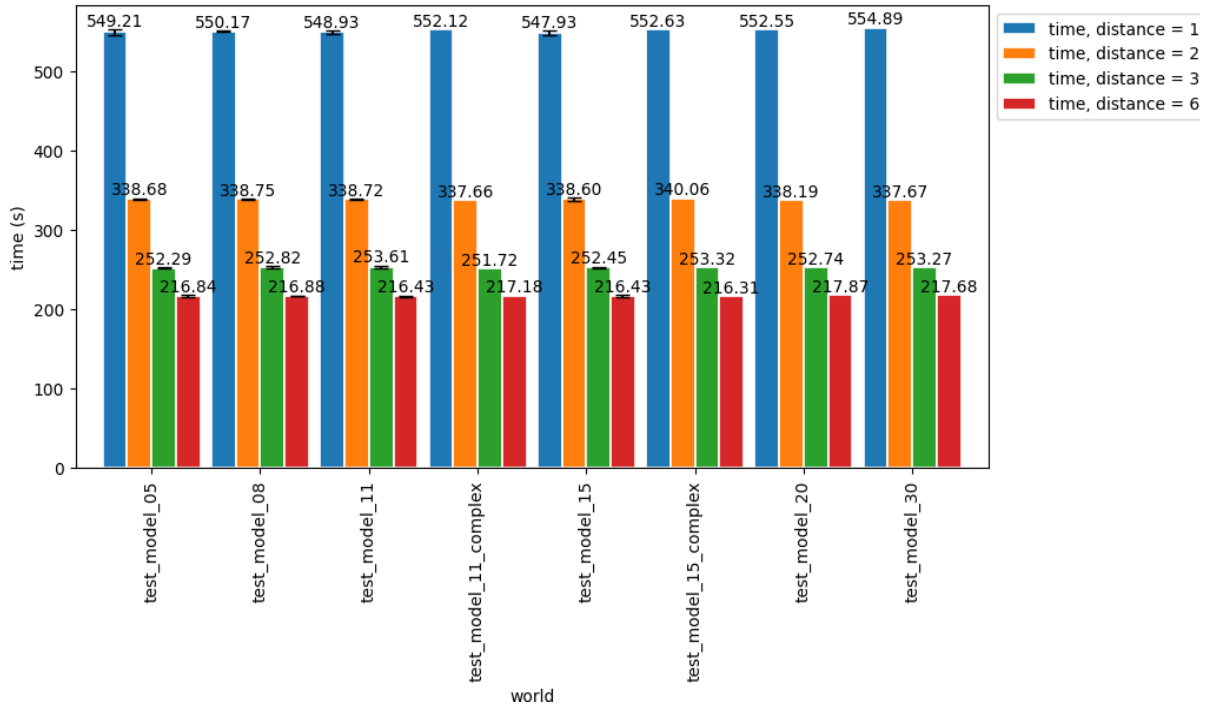
(b) Runtime based on world density.

Figure 6 Evolution of Cohen's $\kappa$ and the execution time of the *Roller Painting* algorithm
as a function of the density of the world and the distance between the robots



(a) $\kappa$ depending on the distance between
the two crawlers.

(b) Runtime depending on the distance
between the two crawlers.

Figure 7: Evolution of Cohen's $\kappa$ and the execution time of the *Roller Painting* algorithm as a function of the distance
between the two crawlers

Then, we observe that the execution time of the *Roller Painting* algorithm is constant for each value of the
number of corrosion zones. This was expected because the algorithm in question is an *a priori* algorithm
and therefore does not depend on the number of corrosion zones. On the other hand, the execution time

depends on the distance $d$ between the two crawlers. As we can see in **Figure 7**(b) the execution time increases when the distance $d$ between the two crawlers decreases. This is because the greater the distance $d$, the fewer moves the crawlers have to make to cover the map. There does not seem to be a linear relationship between the execution time and the distance $d$ between the two crawlers. However, we would have expected that there would be a linear relationship between the execution time and the distance $d$ between the two crawlers. It would be interesting to check if there was no bias introduced during the implementation of the algorithm.
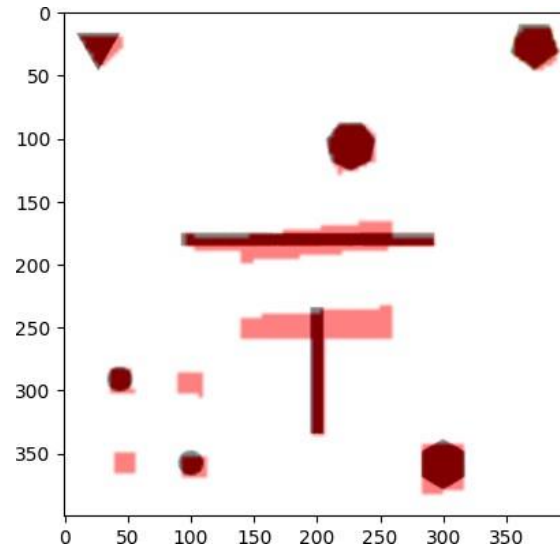


Figure 8: Example of a phantom zone located at the bottom left of the map

We have also introduced two maps with more complex shapes than the base maps. These are visible in figures Figure 3g and Figure 3h.

Unfortunately, we could not, for the sake of time, vary the position of the corrosion zones, as we did with the low-density maps. However, there seems to be no significant difference between complex shaped maps and simple shaped maps. For example, for the maps with 15 forms of corrosion and the map with 15 complex forms of corrosion, the Cohen score only varies by 0.02 on average for a distance $d = 1$ and by 0.04 on average for a distance $d = 6$.

In the rest of this report, we will consider a distance $d = 3$ meters between the two crawlers for the *Roller Painting* algorithm.

## 2.4.2. *Polygonal Investigation* navigation strategy

We then tested the *Polygonal Investigation* algorithm on worlds composed of 5, 8 and 11 corrosion zones. The inspection strategy is based on the results of the *Roller Painting* strategy. As explained previously, we justify this choice by the fact that the *Roller Painting* strategy is the fastest of the *a priori* strategies that we have implemented.
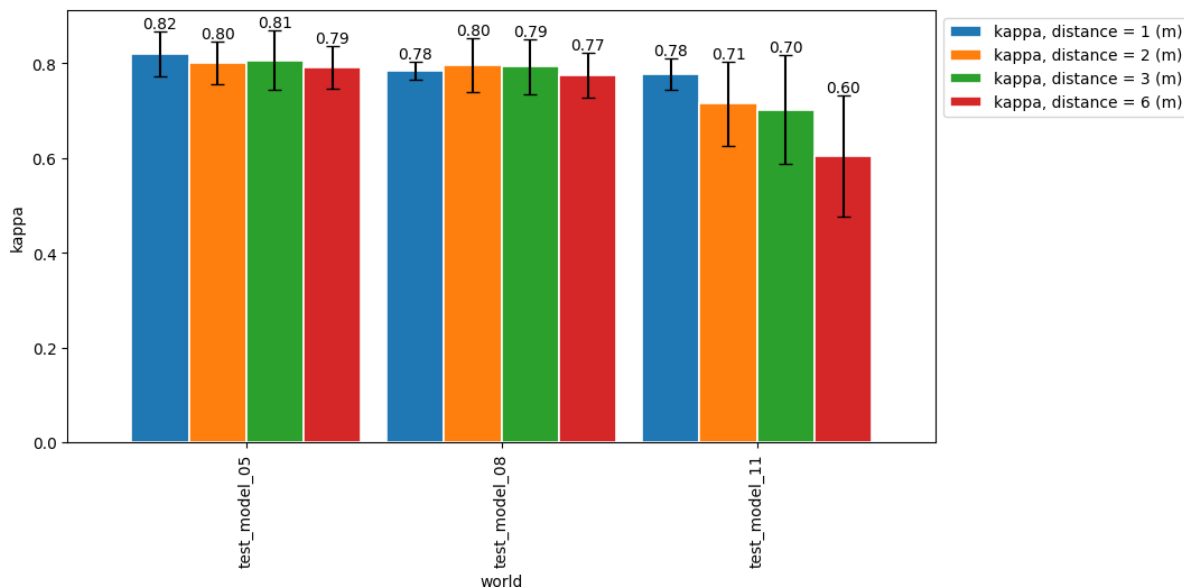
(a) $\kappa$ according to the density of the world.
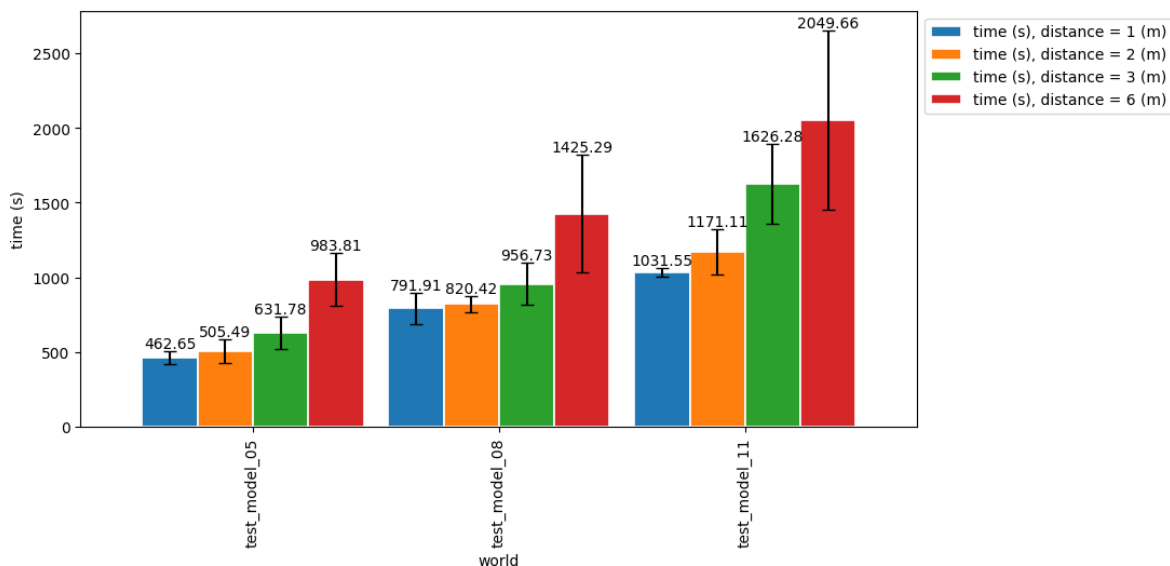


(b Runtime based on world density.

Figure 9: Evolution of Cohen's $\kappa$ and *Polygonal Investigation* algorithm runtime according to the world density for different distances between crawlers with a 4-sided polygon

**Figure 9**(a) shows the evolution of the Cohen score according to the density of the world for each value of $d$ used in the strategy *Roller Painting*. We used a 4-sided investigation polygon. First, we observe Cohen scores relatively independent of distance between crawlers for maps with 5 and 8 corrosion zones. This is an exciting result, because it means that we can use the *Polygonal Investigation* strategy based on the results of the *Roller Painting* strategy using a large distance between the crawlers, and therefore, a very fast *Roller Painting* strategy. Nevertheless, we can observe that for maps with 11 corrosion zones, the Cohen score is impacted by the distance between the crawlers, when the latter increases. We attribute this result to the fact that this map has elongated corrosion zones very close to each other, having the effect of blocking certain rays emitted and received during the polygonal inspection of an area. Polygonal inspection

is therefore naturally impacted by the density of the world. However, we can imagine, when repairing metal structures, that it is more convenient to merge corrosion areas close to each other into a single corrosion area, although this is not considered in our problem.

**Figure 9**(b) shows the evolution of execution time according to the world density for each value of $d$ used in the strategy *Roller Painting*. We used a 4-sided investigation polygon. We observe that the execution time increases with the density of the world in a linear way. This is an expected result, because the *Polygonal Investigation* algorithm has linear complexity as a function of the number of corrosion zones, the latter consisting in traversing all the potential corrosion zones and inspecting them. We also observe that the execution time increases with the distance between the crawlers. Indeed, the greater the distance between the crawlers, the greater the number of phantom zones at the end of the *Roller Painting* navigation strategy, and therefore the greater the number of potential corrosion zones. However, these phantom areas are quickly processed by the *Polygonal Investigation* algorithm. For example, for map 5 with 11 corrosion areas, we get 12 potential corrosion areas with a distance of 1 meter between crawlers after the *Roller Painting* strategy, versus 20 potential corrosion areas with a distance of 6 meters between the crawlers. However, we observe an execution time of 1027 seconds for the first configuration versus 1616 seconds for the second configuration. So, for a 67% increase in the number of potential corrosion areas, we observe a 57% increase in execution time. The performance gain is not very large but is still significant.
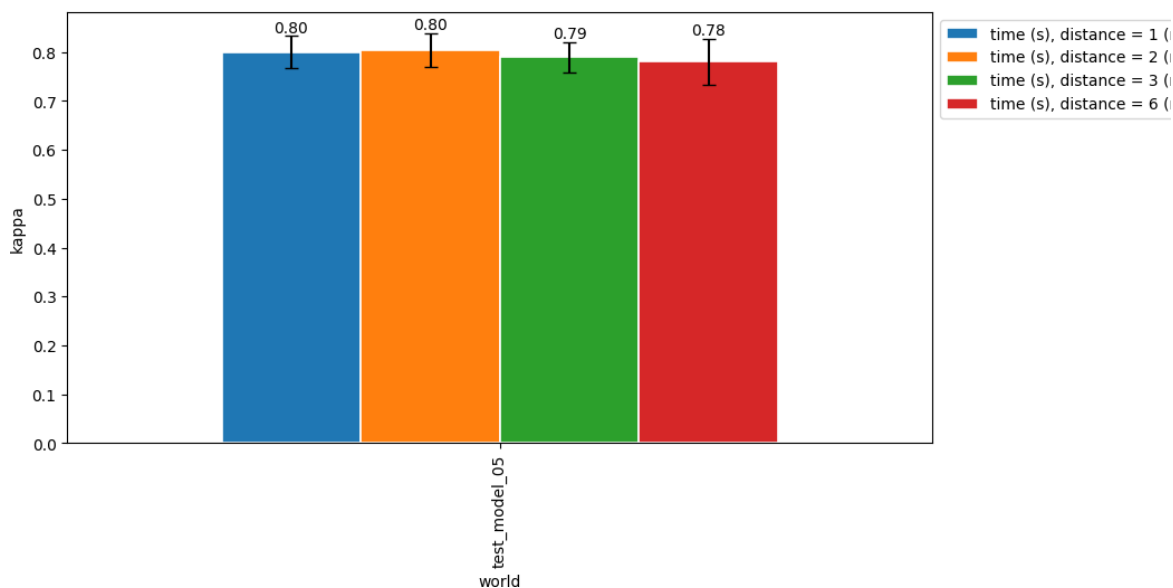


*(a)*  $\kappa$ according to the density of the world.
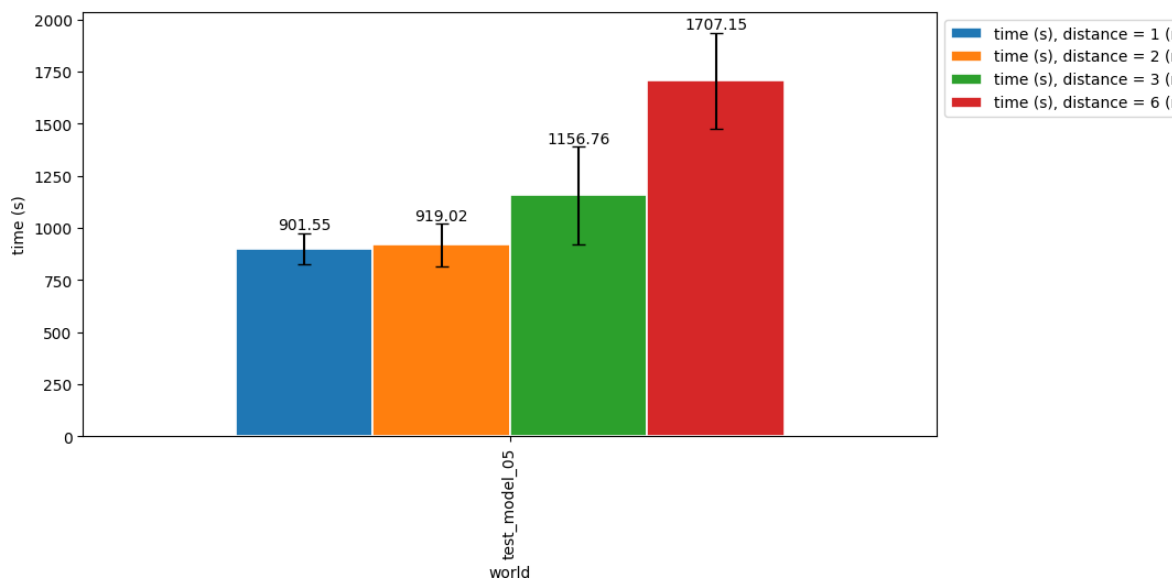
*(b)* Runtime based on world density.

Figure 10: Evolution of Cohen's $\kappa$ and *Polygonal Investigation* algorithm runtime according to the world density for different distances between crawlers with a 6-sided polygon

We also varied the size of the investigation polygon of the *Polygon Investigation* strategy. We present in **Figure 10**(a) the evolution of the Cohen score as a function of the density of the world for map 5, for a polygon with 6 vertices. First, we do not observe a significant improvement in the Cohen score when the size of the investigation polygon increases. On the contrary, we observe an average decrease, although very weak, of the score. In theory, increasing the size of the investigation polygon should make it possible to better approach the convex hull of the corrosion zones, and therefore to obtain a better Cohen score. However, we are limited in our implementation by the resolution used for the discretization of the map. However, for a more precise resolution, we should observe an improvement in the Cohen score.

We present in **Figure 10**(b) the evolution of the execution time according to the density of the world for map 5, for a polygon with 6 vertices. Here, we naturally observe an increase in execution time when the size of the investigation polygon increases.

We would also have liked to vary the number of robots used for the polygonal investigation as well as the number of robot teams. However, we did not have time to implement a solution for managing collisions between robots in this simulation environment. It would be interesting in future work to implement such a solution and to analyse the performance of the *Polygonal Investigation* algorithm with these different parameters. Indeed, the execution time of the *Polygonal Investigation* algorithm should decrease when $k$ and $n$ increase.

## 2.5. Conclusion

In conclusion, this study showed that it is theoretically possible to implement various strategies for mapping corrosion areas with multiple robots probing the structure with transmitted ultrasonic guided waves. The results obtained demonstrate the feasibility of these approaches under the assumption that the existence of a defect on the ultrasonic wave path can be detected reliably.

The first strategy, the *Roller Painting* strategy, made it possible to obtain satisfactory results in very short exploration times. The distance between the robots can be adjusted to optimize the results depending on the density of the inferred corrosion zones. This strategy is particularly suitable for use prior to the *Polygonal Investigation* strategy because it provides a quick approximate view of potential corrosion areas.

In a second stage, the *Polygonal Investigation* strategy, can be used to refine the mapping results, in terms of accuracy. However, this strategy is more sensitive to collisions between robots, and require synchronized planning of the team of robot, including their tether, as demonstrated in deliverable D6.1 (Multi-crawler inspection planning and execution control).

# 3. Long range detection using Ultrasonic Guided Waves

## 3.1.    Introduction

Based on the conclusions of deliverable D3.2 (Defect localization by acoustic signal triangulation and tomography), the developed methodology relies on ultrasonic imaging using guided wave reconstruction to achieve the following objectives:

- Simultaneous localization and geometry inference on a metal plate (autonomous robotic system).

- Defect detection and localization from a robot or robot team.

The most suitable sensor for our application is the EMAT (Electromagnetic Acoustic Transducer) sensor. It fulfills the following requirements:

- Modal selectivity on transmission and detection the SH0 mode with the best possible Signal-to-Noise Ratio (SNR).

- Omnidirectional transmission and reception (360° scanning).

- Contactless, coupling-free measurement.

This section will present the results of both manual and robotic tests for long-range detection of defects and other reflectors.

## 3.2.    Manual long-range detection using Ultrasonic Guided Waves

### 3.2.1.    Tests description

#### 3.2.1.1.    Obstacle detection tests on CETIM's mock-up

In this section, we present the results of the obstacle detection tests on the inspection mock-up prepared by CETIM. As a reminder, the mock-up (presented in the Report D3.2) has dimensions of 2 m x 3 m, with a thickness of 8 mm, including the painted coating with an average thickness of 400 µm. The mock-up is an assembly of several plates joined together by butt-welds and stiffeners. The schematic description of the

structure is shown in Figure 11(a) and the EMAT probe with the manual support for 360° rotation is shown in **Figure 11**(b).

From an acoustic perspective, the obstacles on which waves will reflect include the welds, stiffeners, as well as the four edges of the mock-up. The numerical study of the propagation of guided waves in SH modes (presented in the Report D3.2) has shown that the edges and the stiffeners have a better wave reflection coefficient due to their geometric discontinuities. When interacting with a weld, only a small portion of SH waves is reflected, while a significant portion continues to propagate through.

To better distinguish potential wave echoes from different obstacles during these tests, the probe was positioned in a corner of the mock-up, avoiding equidistance to obstacles (**Figure 11**(a)).
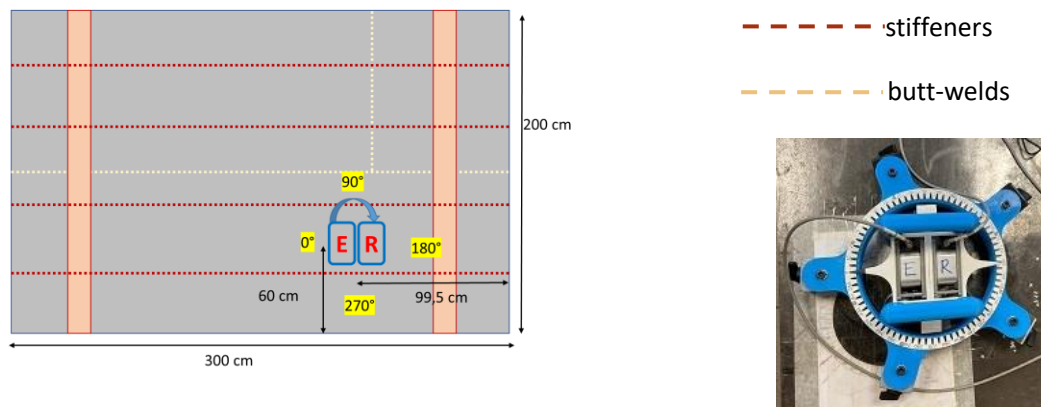


(a) Schematic description of test configuration on the mock-up. The probe is placed to different distances to the main obstacles (edges, stiffeners)

(b) The EMAT probe and support for manual rotation 360° scan

Figure 11: Description of the tests for obstacles detection on the mock-up

The parameters of ultrasonic measurement are presented in **Table 2**.

Table 2: Ultrasonic measurement parameters

| Parameters of excitation | |
|---|---|
| Frequency | 200 kHz |
| Excitation voltage | 1200 V |
| N° of cycle | 2 |
| Pulse Repetition Frequency | 25 Hz |
| Parameters of reception | |
| Averaging | 16 |
| Windows length | 1636 µs (maximum capacity of hardware) |
| Sampling rate | 10 MHz |

The scan result is presented in the form of an image, as shown in **Figure 12**(b). The center of the circle corresponds to the probe position. The mock-up plan is also included to verify the consistency of the obstacle detection.

- As cited above, the edges are detected with high signal-to-noise ration.
- Several stiffeners and butt-welds have been identified, exhibiting a lower contrast.
- Some spots designated as undesired echoes occur because, for each scan angle, the probe generates wave in two opposite directions. As depicted in **Figure 12**(a), the measurements at 0° and 180° are nearly equivalent for the significant echoes.
- There is a dead zone approximately 10 cm from the probe. This zone corresponds to the emission signal that can be observed in the signals in **Figure 12**-a.
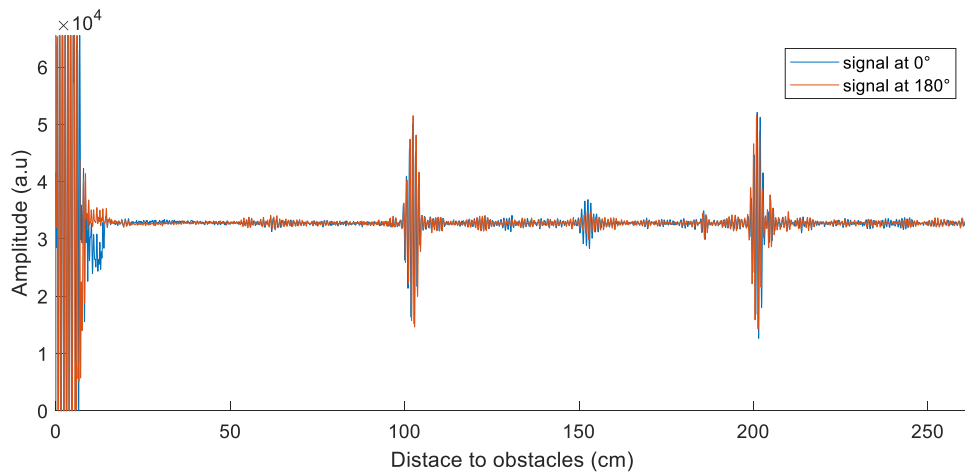


(a) Example of A-scan signals showing the symmetry of wave generation in two opposite directions. Velocity of $SH_0$ mode = 3200 m/s
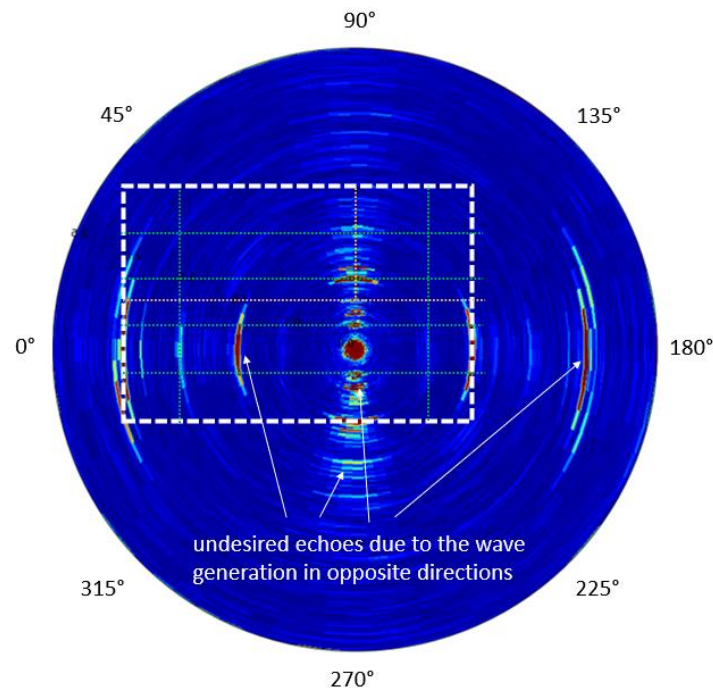


(b) Reconstructed image from 360° scan data

Figure 12: Result of test on the mock-up for obstacles detection

### 3.2.1.2. Results

The tests were carried out on a steel plate 1000 x 1250 x 6 mm³ containing artificial thickness losses (**Figure 13**(a) and (b)).

- Reflector 1: rectangle shape, 92 x 184 mm2 and 2 mm depth (33% of loss)
- Reflector 2: circular shape, Ø= 46 mm, and 3 mm depth (50% of loss)
- Reflector 3: circular shape, Ø= 30 mm, and 4 mm depth (67% of loss)

The probe was placed in a corner and on the opposite face with respect to the artificial defects. To reduce the effect of the symmetry, we combine two scans at different positions, separated by a small enough distance (less than the width of spot) and at a preferable angle between 30° and 60° with respect to the edges. With each of the scans, we get a SAFT[1] image of the plate. The next step is to multiply the two images: by doing this, all the spots corresponding to real defects or edges will still appear on the new image (because they appear in the two scans), while the symmetric spots of each scan will disappear, because they are in different positions in each of the two scans (and thus these spots are multiplied by zero).

The parameters of ultrasonic measurement are identical to those presented in **Table 2**.

Based on the results presented in the **Figure 13**(c):

- First, the algorithm for suppressing the symmetry problem was efficient. Undesired echoes from the edges were almost removed from the final image.
- The edges of the plate were well detected with high resolution.
- The indicators 1 and 2 were detected by their edges regarding the direction to the probe, with an acceptable signal-to-noise ratio.
- In the case of the indicator 3, a low signal-to-noise ratio trace is observed at the position of the indicator but it's not evident to distinguish that one from another significant amplitude spot located nearby, probably related to the symmetry of the wave generation.
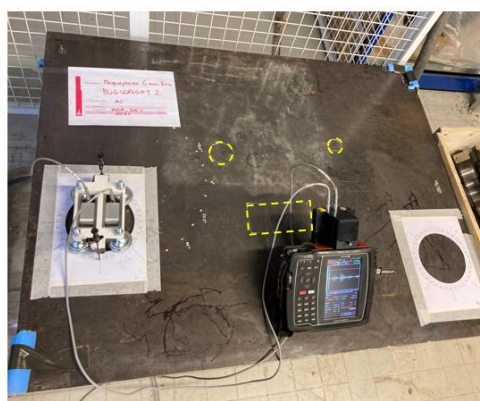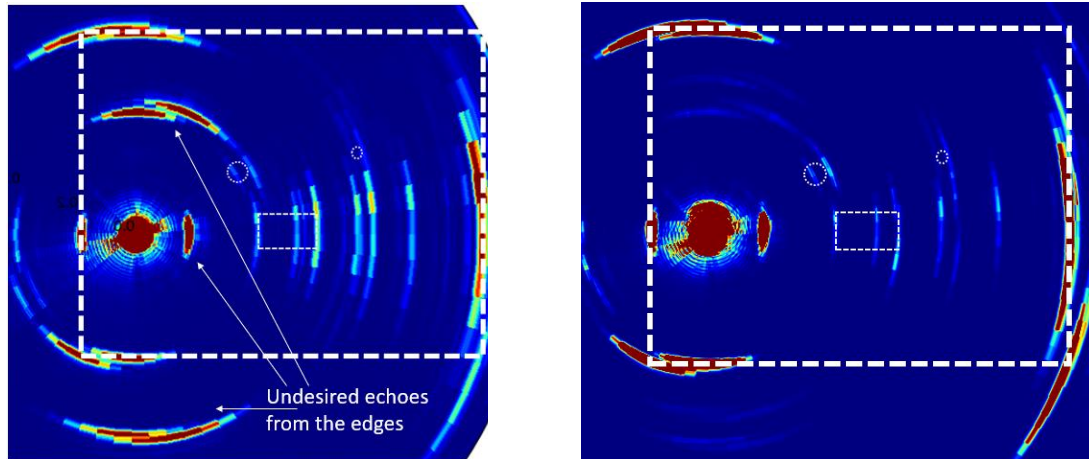


(a) Experimental setup for testing thickness loss localization
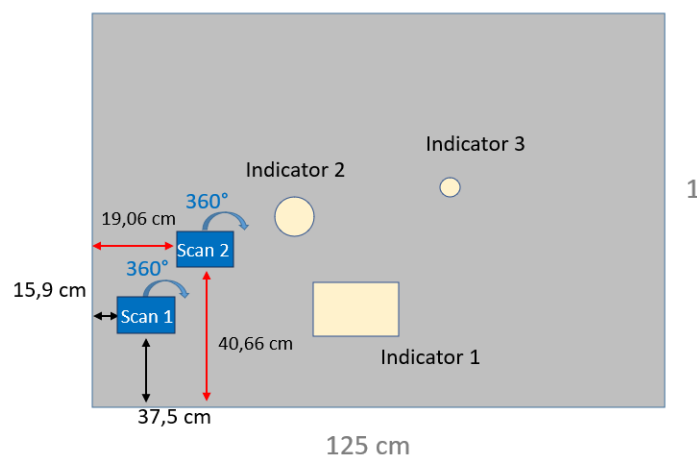
(b) Schematic description. Measurement at two positions to reduce effects of the symmetry

---

[1] Synthetic Aperture Focusing Transform: algorithm described in deliverable 3.2.

(c) Image reconstructed from one 360° scan data.

(d) Image obtained by multiplying two images of two scans for the suppression of undesired echoes due to the symmetry of wave generation.

Figure 13: Tests of artificial defects detection in a 6mm steel plate

## 3.3. Robotic long-range detection using Ultrasonic Guided Waves

### 3.3.1. Robotic solution description

To perform acquisitions with the probe mentioned in section 3.1, we need a solution that enables movement on the structure. Furthermore, to facilitate a 360° angular scan, a solution allowing the probe to rotate must be employed.

### 3.3.2. Incorporating the probe on the robot

To enable the probe to move from point A to point B, we utilize a robot from the NAVIC JIREH brand. Originally designed for movement on ferromagnetic structures, we had to make mechanical adjustments to integrate our probe into the robot. Concerning the robot's structure, the only viable option was to position the probe at the front. The design and production of various mechanical integration components were executed using the plastic additive method. In integrating the probe onto the robot, we assumed that the latter would undergo rotational movement to facilitate an angular scan. This aspect will be elaborated upon later.



Figure 14: NAVIC JIREH and probe

### 3.3.3. Motorization of the probe

We initially determined the minimum torque necessary to enable the rotation of the probe. This minimum torque of 5 Nm was measured on the model present at CETIM. This value is influenced by the material of the structure, its thickness, and the air gap between the two permanent magnets of the probe and the surface to be inspected.

To address this challenge, we employ a 1.3 Nm stepper motor in conjunction with a wheel/pinion system, featuring a reduction ratio of 1/8th. This combination yields a theoretical torque of approximately 10 Nm. This 10 Nm value provides a margin for the maximum torque, thus preventing mechanical blockage resulting from insufficient motor torque.
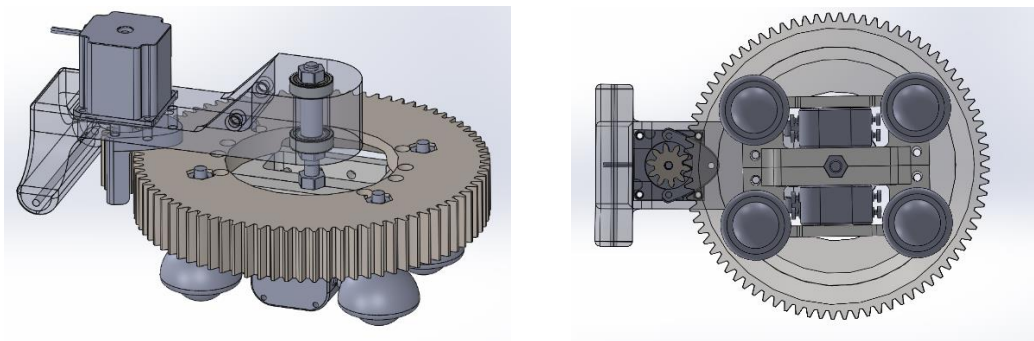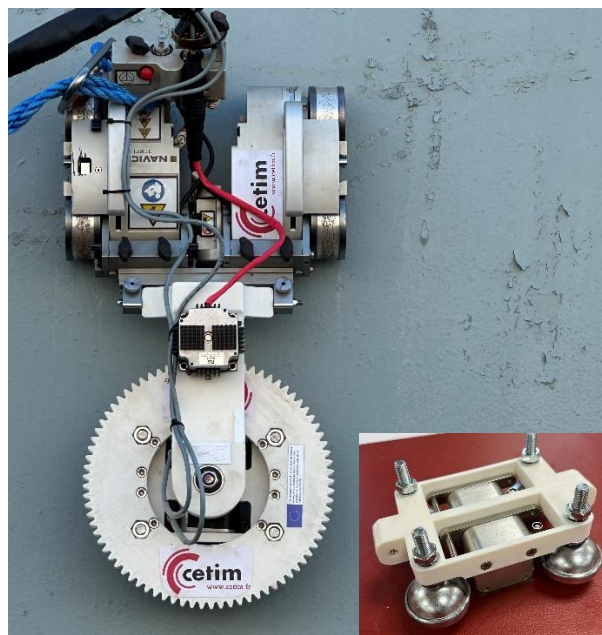


Figure 15: CAD of the wheel/pinion + motor system



Figure 16: Photograph of the robot with the motorized probe

## 3.3.4.    Control and Acquisition

To control the stepper motor, an Arduino control board and a Gecko motor driver are utilized. The control board facilitates the integration of the different components of the system, which, in turn, enables synchronization with the acquisitions conducted by the Innerspec acquisition system.
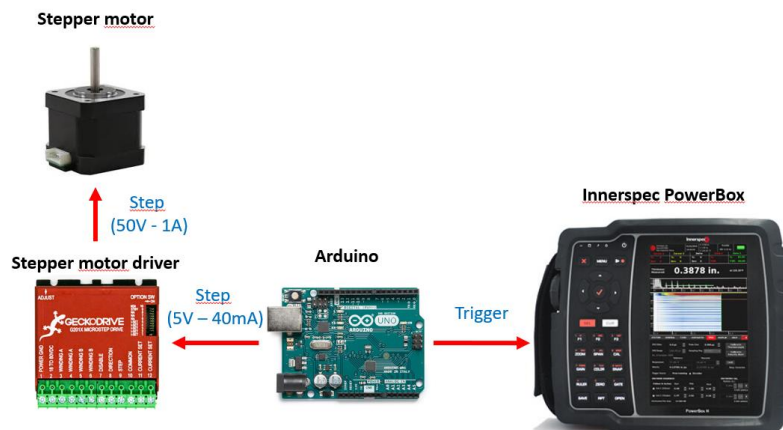


Figure 17: Schematic diagram

To conduct a full angular scan acquisition, the motor is incrementally rotated 80 times by 4.5° each, enabling a comprehensive 360° acquisition. In each angular increment, the control board transmits the rotation command to the motor and then sends a trigger signal to the acquisition system. Each increment has a total duration of 20 seconds. Consequently, the overall acquisition time is nearly 25 minutes. This duration is not a physical limitation but rather a constraint imposed by the slow acquisition system. If the acquisition system were faster, the complete acquisition time could be reduced to 3 minutes.

Table 3: Characteristics of data acquisition using the robotic setup

| | |
|---|---|
| **Angular resolution** | 4,5° |
| **Number of acquisitions for 1 round** | 80 |
| **Time of an acquisition** | 20 sec |
| **Total time for 1 lap** | Around 25 min. |

## 3.3.5.    NRP Berrio test descriptions

The tests were conducted on the "NRP Bérrio" ship during the integration week in Lisbon from 11 to 15 September 2023.
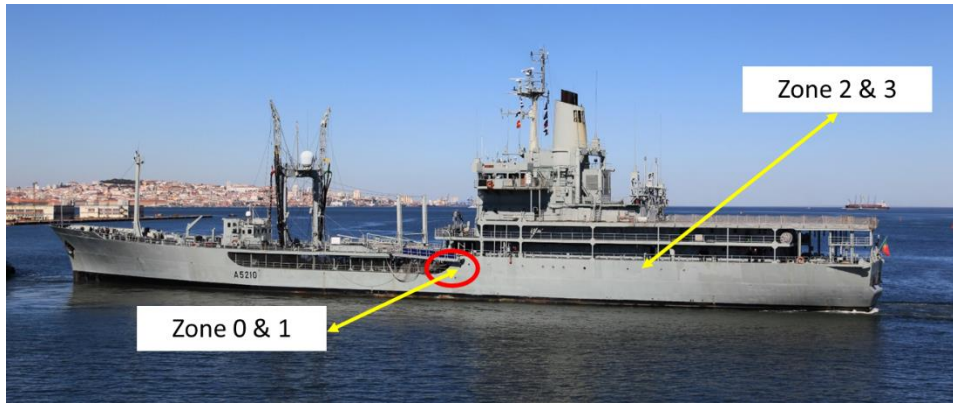
Figure 18: NRP Bérrio [18]

4 different zones were considered in this test campaign (zones 0 to 3). The following table summarizes all these tests:

Table 4: Tests description

| Controlled zones | Description | scans performed | Observations |
|---|---|---|---|
| Zone 0 |  | **360° Scan:** 3 angular scans performed.<br><br>*Objectives*: detection of reflectors (stiffeners, edges, welds)<br><br>**Linear Scan:** a line scan over 1.5m (0.06 m/s) between the two stiffeners<br><br>*Objectives: B-scan* | - S/N correct.<br>- high electromagnetic noise |
| Zone 1 |  | **360° Scan:** 3 angular scans performed.<br><br>*Objectives*: detection of reflectors (stiffeners, edges, welds)<br><br>**Linear Scan:** a line scan over 1.5m (0.06 m/s) along the longitudinal weld<br><br>*Objectives: B-scan* | - S/N very low<br>- severely deteriorated coating<br>- high electromagnetic noise |

| | | | |
|---|---|---|---|
| Zone 2 |  | **360° Scan:** 6 angular scans performed.<br><br>*Objectives*: detection of reflectors (stiffeners, edges, welds) & metal impact<br><br>**Linear Scan:** a line scan over 1.5m (0.06 m/s) along the longitudinal weld<br><br>*Objectives: B-scan* | - S/N very low<br>- severely deteriorated coating<br>- high electromagnetic noise |
| Zone 3 |  | **360° Scan:** 1 angular scan performed.<br><br>*Objectives*: detection of reflectors (discontinuities, welds)<br><br>**Linear Scan:** a line scan over 1.5m (0.06 m/s) along the longitudinal weld<br><br>*Objectives: B-scan* | - S/N acceptable<br>- high electromagnetic noise (corrected by switching off the motor power supply and applying manual rotation) |

## 3.3.6. Results
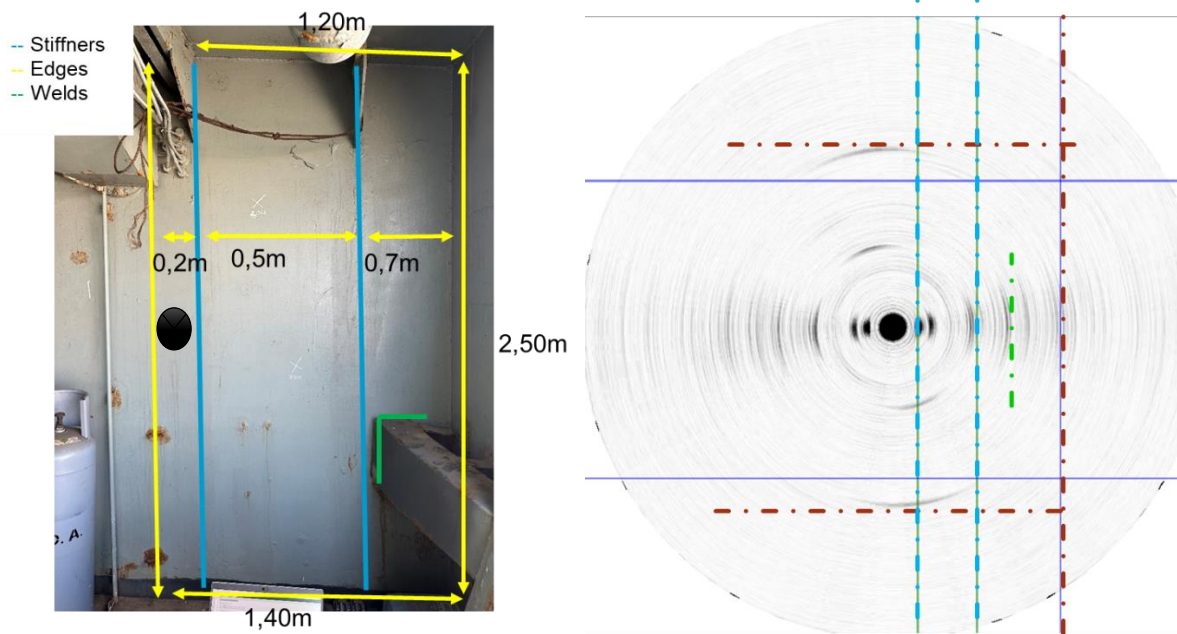
## ZONE 0 – ANGULAR SCAN



**Figure 19: Example of an angular scan result from zone 0**
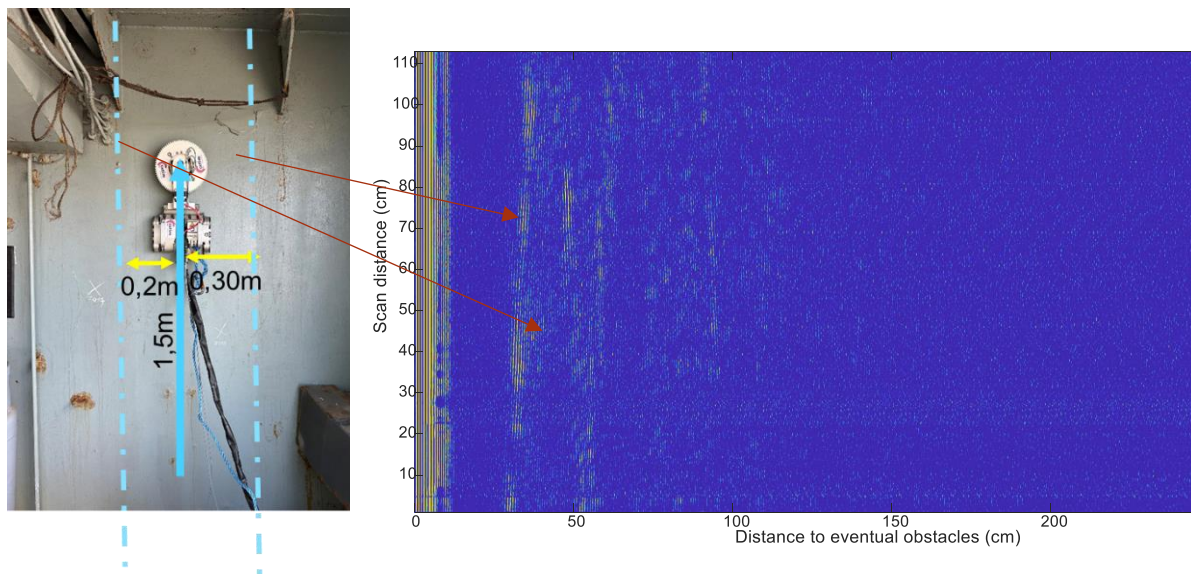
## ZONE 0 – LINEAR SCAN



Figure 20: B-Scan result from zone 0 (0.06 m/s)
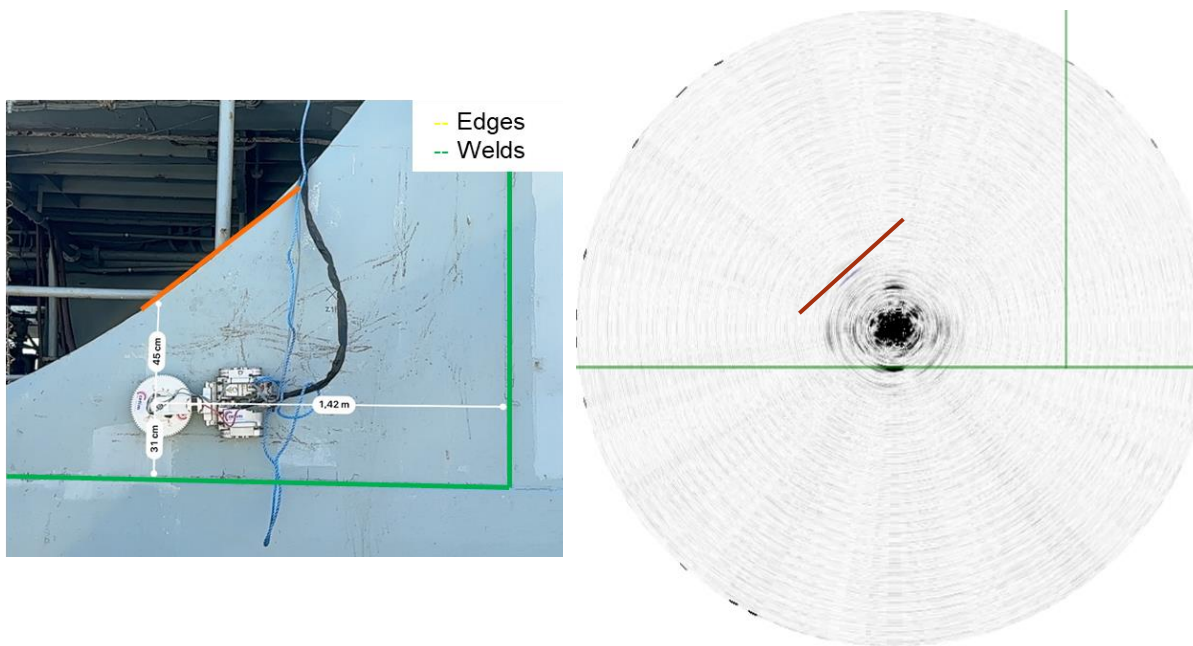
## ZONE 1 – ANGULAR SCAN



Figure 21: Example of an angular scan result from zone 1
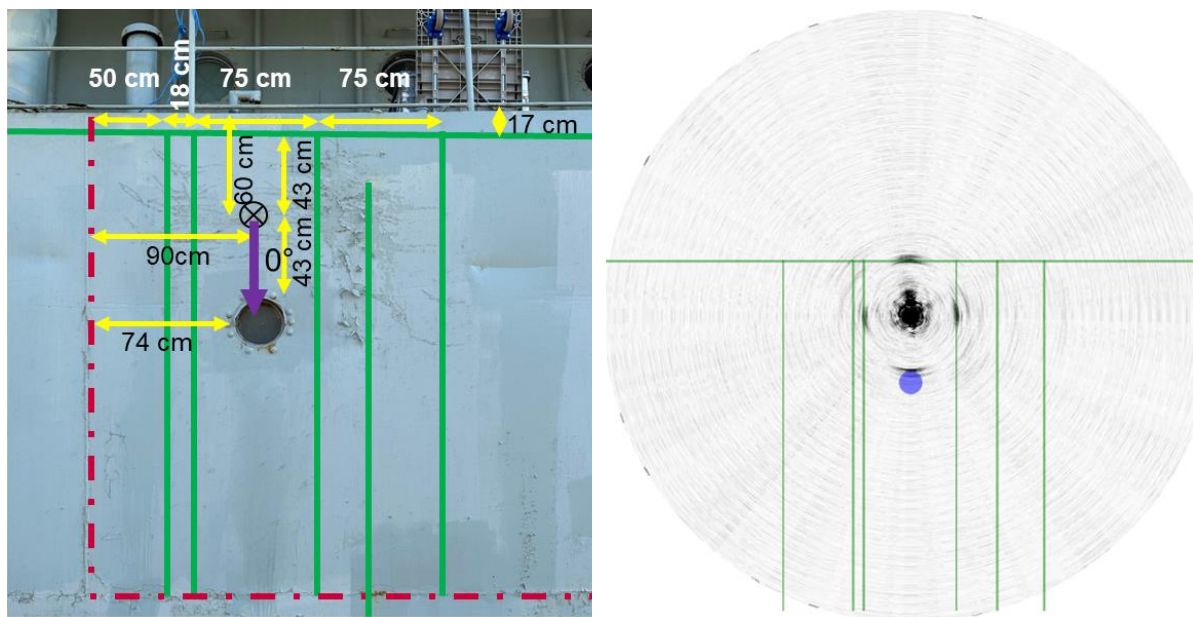
## ZONE 2 – ANGULAR SCAN



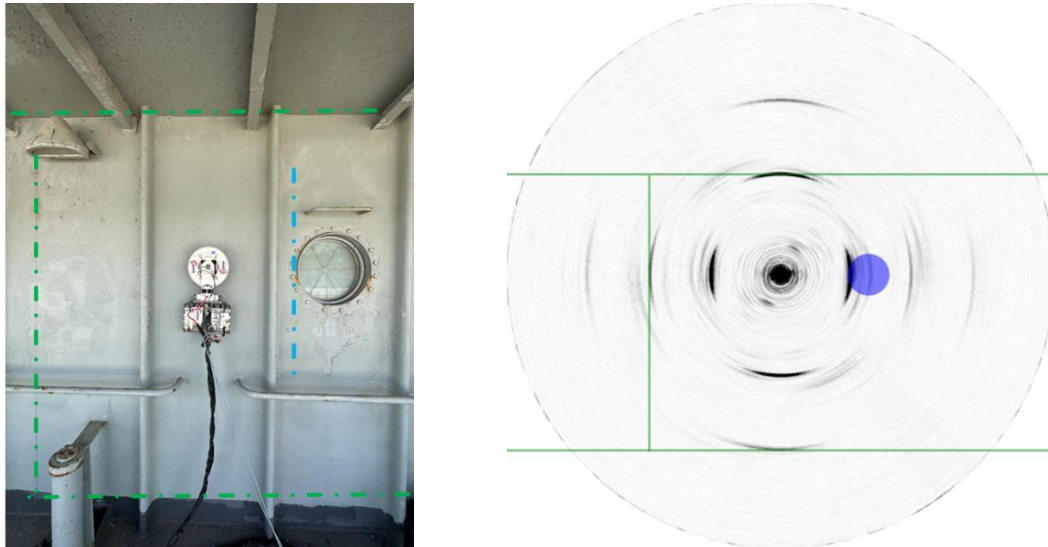Figure 22: Example of an angular scan result from zone 2

## ZONE 3 – ANGULAR SCAN



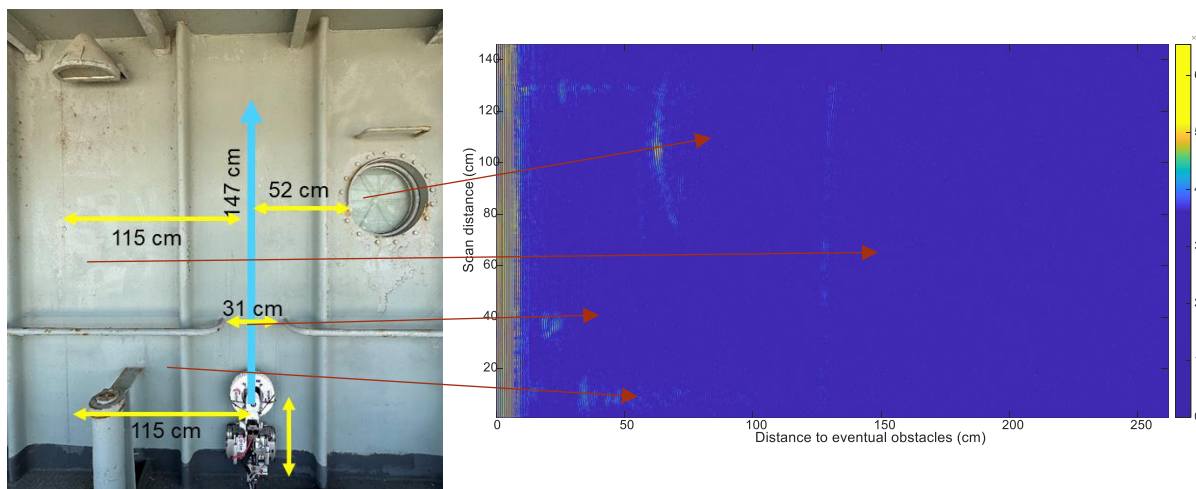Figure 23: Example of an angular scan result from zone 3

## ZONE 3 – LINEAR SCAN



Figure 24: B-Scan result from zone 0 (0.06 m/s)

## 3.3.7.  Summary

Table 5: Summary of results

| Controlled zones | Scans performed | Results |
|---|---|---|
| Zone 0 | 360° scan | stiffeners, welds, edges: OK |
| | Linear scan | Stiffeners: OK (with high electromagnetic noise) |
| Zone 1 | 360° scan | Edge: OK<br>Longitudinal weld: OK<br>Vertical weld: NOK (low S/N and high electromagnetic noise) |
| | Linear scan | NOK: (low S/N and high electromagnetic noise) |
| Zone 2 | 360° scan | Stiffeners, welds, discontinuity: OK |
| | Linear scan | NOK: (low S/N and high electromagnetic noise) |
| Zone 3 | 360° scan | Stiffeners, welds, discontinuities: OK<br><br>Impact : NOK (SH0 non-sensitive) |
| | Linear scan | Stiffeners, welds, discontinuities: OK |

## 3.4. Long rang defect/obstacle identification using Super Resolution

As this step has not yet been carried out on BUGWRIGHT2's data, the results of another similar study will be presented to describe the general approach envisaged.

The images obtained after scanning and TFM (Total Focusing Method) reconstruction are difficult to interpret due to the multiple echoes received from obstacles. The echo signatures obtained from obstacles and defects should not be the same. Based on this hypothesis, we are considering using a super-resolution technique based on Deep Learning to differentiate between the various signatures and enhance image interpretation.

Here, super-resolution visualization of subwavelength defects via deep learning-enhanced ultrasonic beamforming: In a proof-of-principle study [19], Song and Yang apply a super-resolution algorithm to improve the quality of TFM mappings.
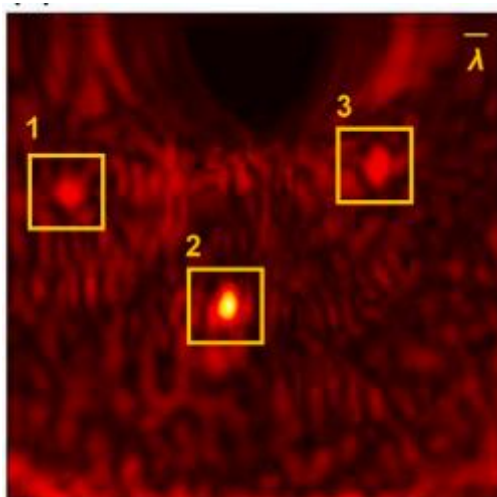
## 3.4.1. Method introduction



Figure 25: Example of a real image obtained with TFM **[19]**

Figure 36 shows an example of an image obtained with TFM in a real experiment. We can see that although defects can still be distinguished, marked with bounding boxes, it's much more complicated to determine which part of the image corresponds to a defect and which to an intact area, due to noise. To improve image quality, Song and Yang use a Deep Learning super-resolution algorithm, which is explained below.
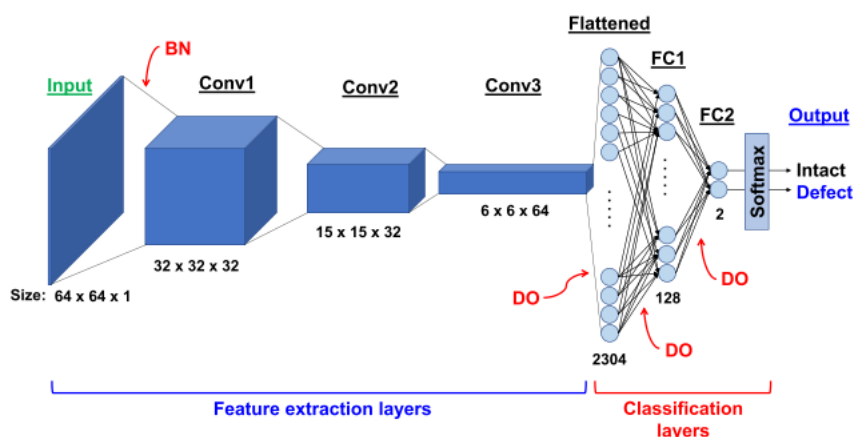


Figure 26: Architecture of the detection network **[19]**

Initially, a sliding window of size 64x64 is passed over the TFM image, allowing to obtain 64x64 image patches. On each of these patches, a first neural network, the detection network (Figure 26), is applied. This network is a classification network: for each image patch, it returns whether it contains a defect or represents an intact area.

Then, the image patches classified as having a defect are input into a second neural network (a U-Net type encoder-decoder, Figure 27), which returns the image in higher quality, with more precise defects (similarly to a segmentation network).
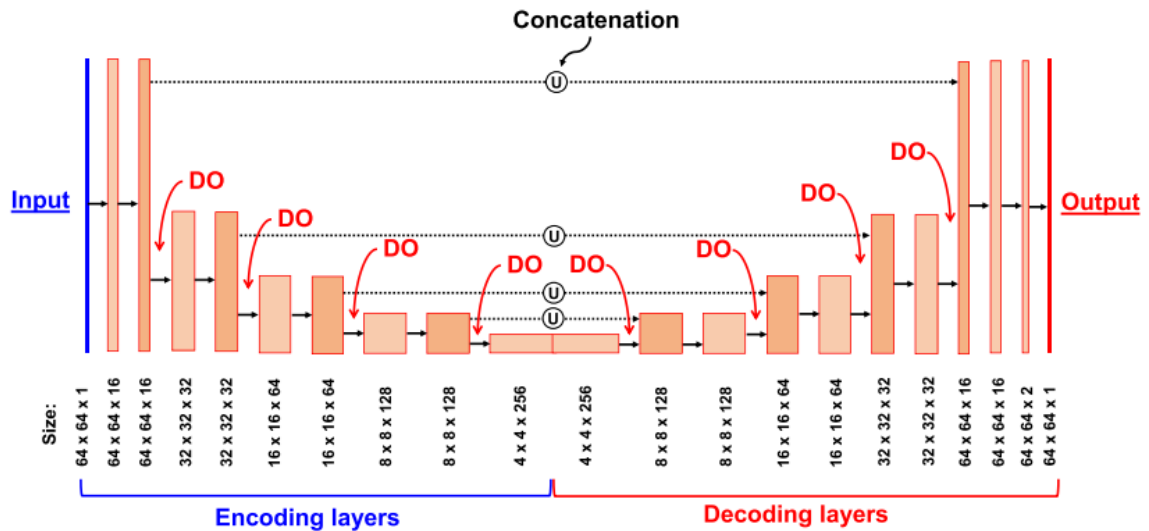
Figure 27: Architecture du réseau de Super résolution **[19]**

The method is summarized in Figure 28.
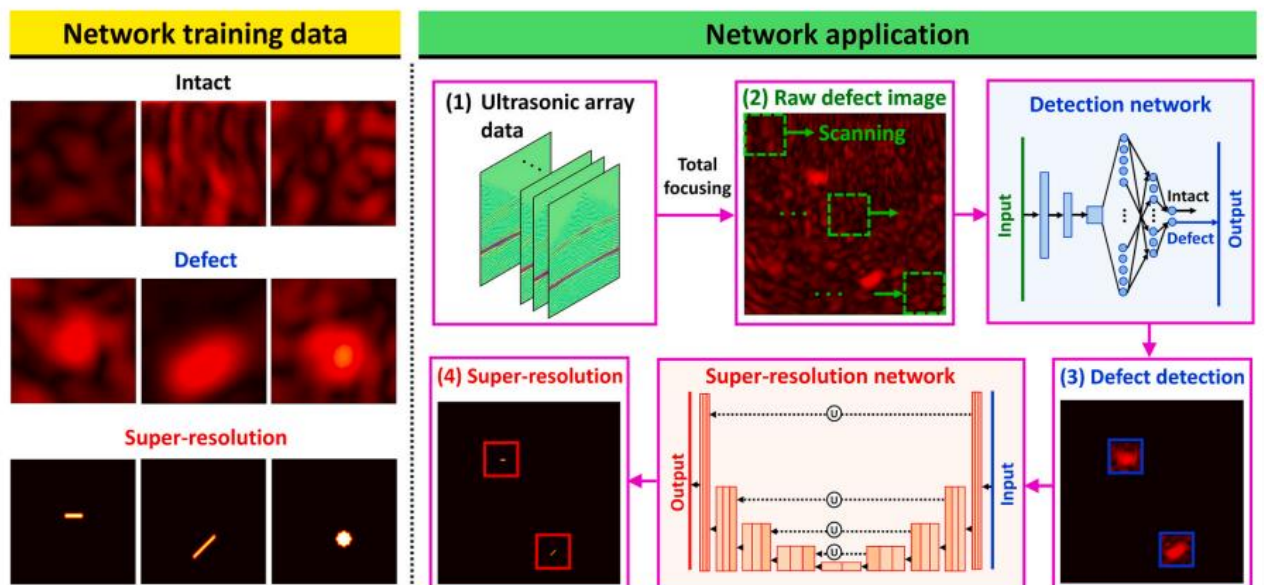


Figure 28: Summary of the method **[19]**

The two neural networks are trained separately. The detection network is trained with image patches labeled as having a defect or not (the first two rows of images of Network training data in **Figure 28**), while the super-resolution network is trained with image patches showing a defect as well as the associated super-resolution image patches, labeled pixel by pixel (the last two rows of images of Network training data in **Figure 28**). Data augmentation is also applied to the image patches (random cropping, horizontal flipping, random zooming, random rotation) (Figure 29).

Figure 29: Methods of data augmentation **[19]**

### 3.4.2. Implementation

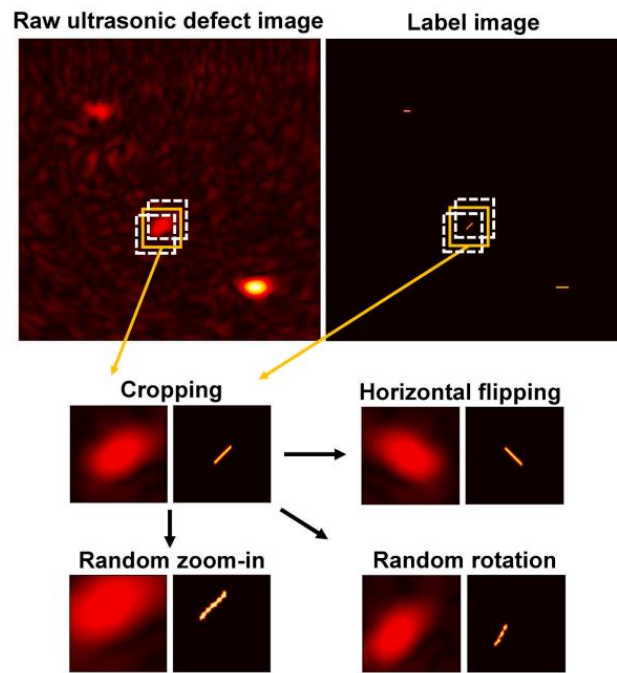As training images, initially, we use images from TFM, made with previous simulations. An example of an image is on the **Figure 30**.
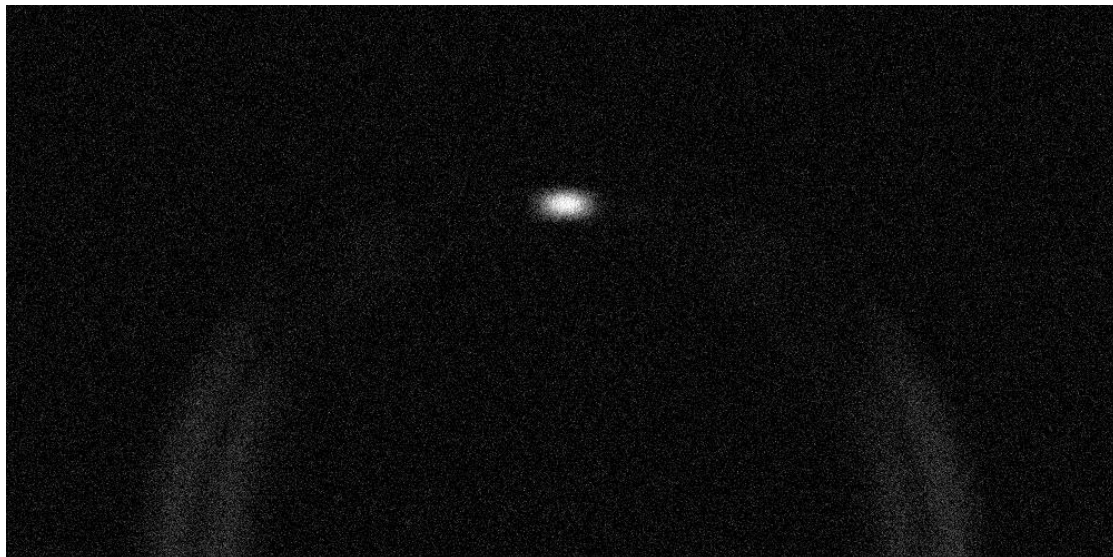


Figure 30: Example of a training image

From these various images, small image patches are extracted of size 64x64, labeled as containing defects or not (**Figure 31** and **Figure 32**).
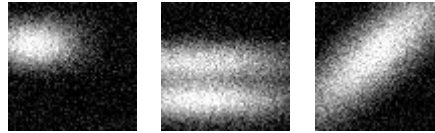
Figure 31: Some examples of image patches with defects



Figure 32: Some examples of image patches without defects

The detection network, with an architecture similar to that of Song and Yang [19], was thus trained with these images.

To train the super-resolution network, we use image patches with defects, as well as their associated 'masks'. The image we want to obtain as output is created manually Figure 33.
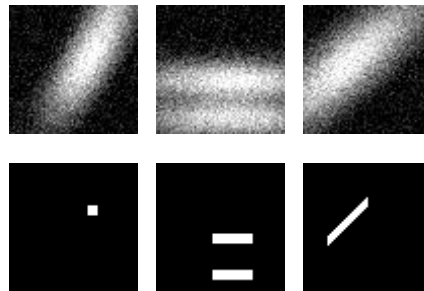


Figure 33: Some associations of image patch (top) – mask (bottom)

Then the training is started on a reduced database about 250 images taken from simulations, but with only 5 different stains (maxima of the probability of detection), from which 50 different images are extracted through data augmentation.
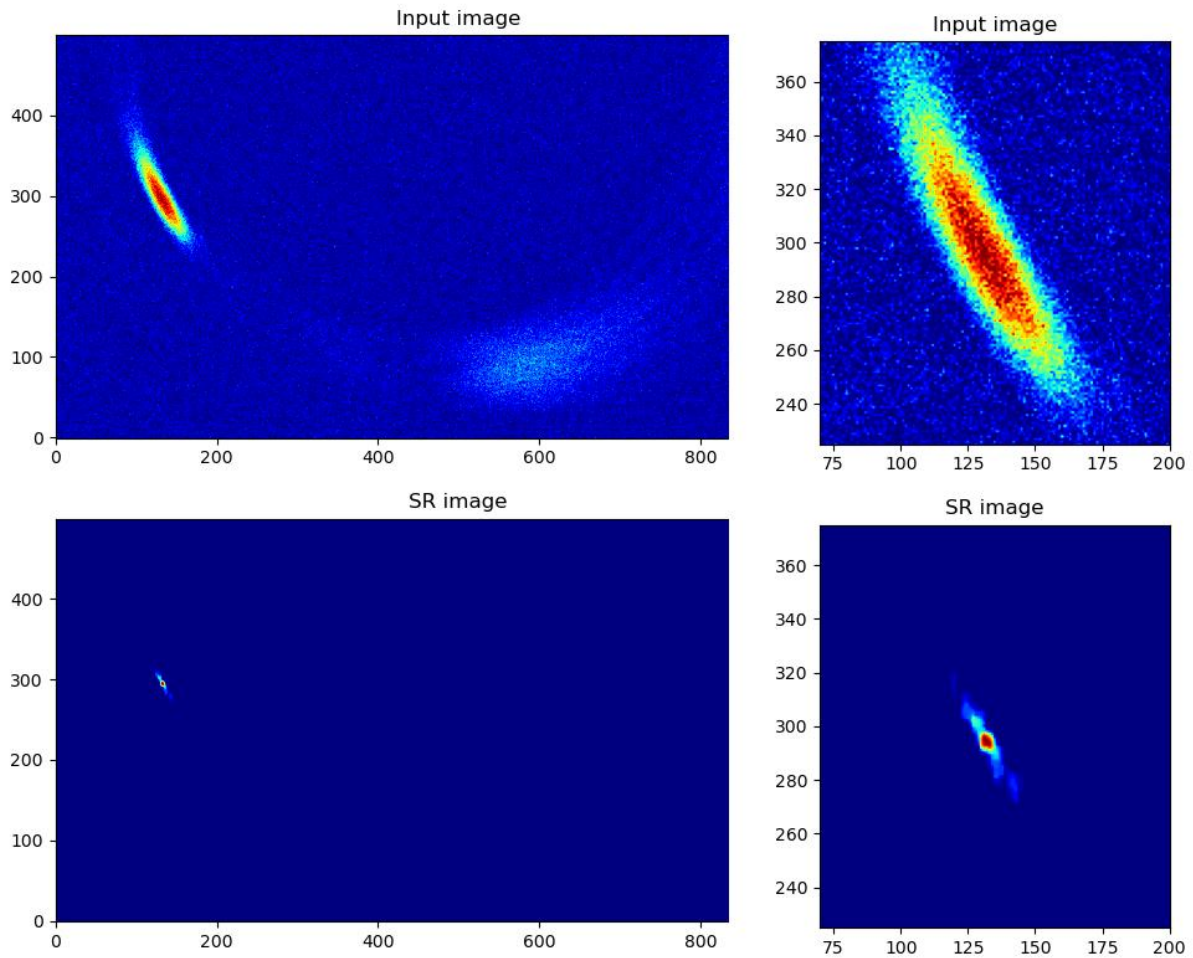
Figure 34: Result of the super-resolution on a first example (zoom on the right)

From the trained models, Song's algorithm is applied to new images. **Figure 34** shows an example where it works well, with the large stain being well reduced to a stain that is roughly the size of the defect and the noise being removed. In **Figure 35**, it works less well, especially the two defects on the side: this is due to the fact that the training database is very limited, and it does not contain stains as stretched as the one on the left, hence it does not produce a satisfactory output.

To achieve better results, it would be necessary to create a substantial database from many different simulations or acquisitions.

Figure 35: Result of the super-resolution on a second example (zoom on both sides)

## 3.5.    Conclusions & perspectives

This section of the deliverable 3.3 summarizes the work carried out in task 3.3 "Robotic long-range detection using Ultrasonic Guided Waves." The main conclusions are as follows:

- EMAT sensors used in the present work confirm their suitability for robotic scanning, specifically the contactless and free-coupling generation of the SH0 mode and its omnidirectional reception.
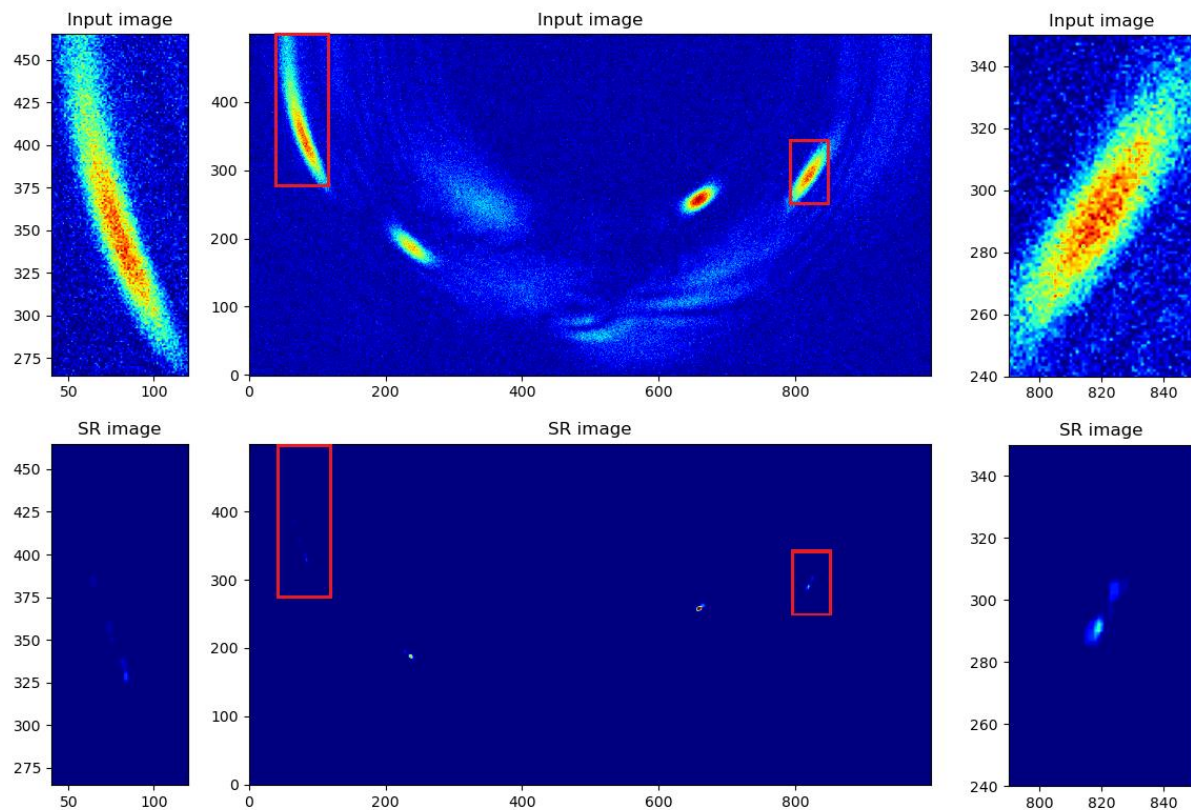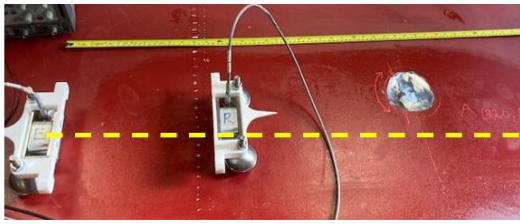
- Angular scan results show improvement in the imaging resolution of discontinuities (edges, welds, stiffeners, etc.) by the SAFT algorithm. However, images are impacted by a poor Signal-to-Noise Ratio (SNR) and electromagnetic noise, which will be corrected after revising the electrical insolation between the motor controller and the ultrasonic acquisition system.

- B-scans are more affected by electromagnetic noise because the Signal-to-Noise Ratio (SNR) is inherently lower. Nevertheless, when noise levels are low, linear scans offer an interesting opportunity to image the length of discontinuities and/or defects. Optimization of instrumentation to improve the Signal-to-Noise Ratio (SNR) and reduce electromagnetic noise is planned.

- As shown in the previous section 3.2, the SH0 mode is very efficient for long-range transmission and detection of reflectors, but it is very insensitive when the thickness variation is progressive (e.g., loss of thickness due to corrosion). In order to improve the corrosion detection performance, initial transmission tests using the SH1 mode have been conducted and confirm the sensitivity of this mode (**Figure 36**). Nevertheless, its stronger dispersion and attenuation makes it a more challenging candidate in terms of propagation distance and signal interpretation.

- Multiple scan results can be combined to represent the results of the scan of the entire structure.

- Super resolution using AI image processing will be applied to BW2 results.

EMAT Emitter          EMAT Receiver
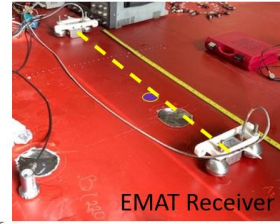
EMAT Emitter

a/ Measurement of transmission in an undamaged zone

EMAT Receiver
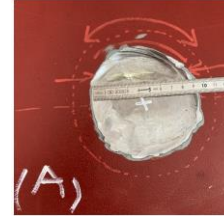
b/ Measurement of transmission through a defect (machined by grinding, $\Phi$~80 mm, $h_{max}$ = 6 mm)
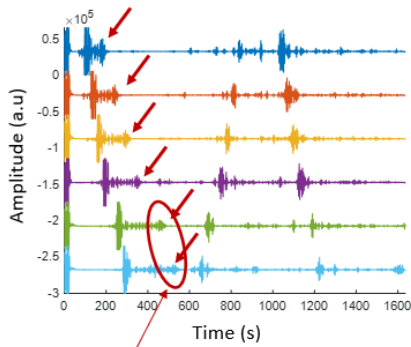
Presence of SH1 mode

c/ Measured signals as function of receiver position in the undamaged zone
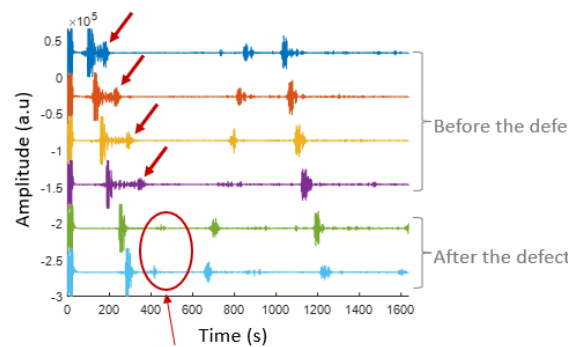
Disappearance of SH1 mode

d/ Measured signals as function of receiver position in the zone with defect

Figure 36: Defect detection in the mock-up by $SH_1$ wave in Transmission

# 4. Long-range defect detection through transmission using Machine Learning

The ability to identify defects, particularly from long ranges, is a critical aspect of the Autonomous Robotic Inspection of ship hulls and other large metal infrastructures. Machine learning (ML), with its ability to process vast amounts of data, recognize patterns, and adapt to new information, emerges as a potent tool for long-range defect detection. Within this section, we will continue exploring the feasibility of long-distance guided waves and potential integration of machine learning methodologies into long-range defect detection through transmission. We will delve into how ML can be harnessed for defect detection and examine its implementation for defect mapping on large metal structure.

In this section, we include results acquired in transmission waves in two application contexts. The first one is photovoltaic modules, the second one is metal plates. The application to photovoltaic panels was considered as a first application due to the practicality of getting access to damage solar panels (common occurrence due to logistics or weather events) and their manipulation, when metal plates are heavy and damaged infrastructures are rare.

## 4.1. Ultrasonic guided waves for faster defect detection

Ultrasonic guided waves offer a promising method for long-range mechanical defect identification [20]. This approach was extensively studied in the context of thin-film solar photovoltaic modules. A significant part of this section has been included in the Ph.D. thesis of Dicky Januarizky Silitonga, within his Ph.D. degree at the Georgia Institute of Technology.

The importance of defect identification in solar panels cannot be overstated. Defects can drastically diminish a panel's performance, resulting in decreased energy production and efficiency [21]. Undetected defects might escalate into expensive repairs or replacements, impacting the return on investment and extending the payback duration of solar PV systems [22].
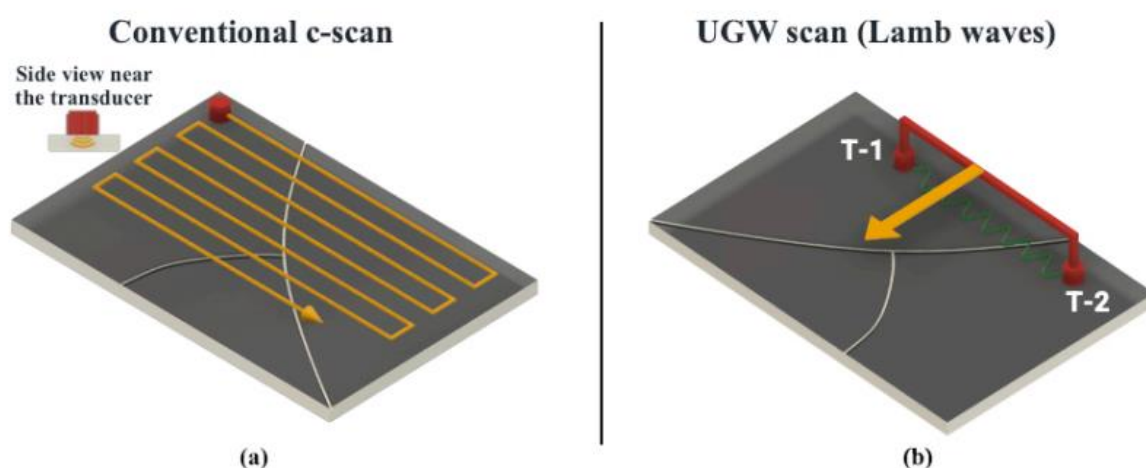


Figure 37: Illustrations of (a) the conventional C-scan and (b) the Lamb waves scan

Lamb waves are a type of elastic wave that propagates in thin plates and is characterized by a combination of longitudinal and transverse vibrations that travel along the material, often used in nondestructive testing

for detecting defects [23]. Using the Lamb waves scan boasts several unique benefits over the conventional C-scan. As depicted in **Figure 37**, the Lamb waves scan offers comprehensive area coverage, a marked improvement over the traditional C-scan method. This advantage, bolstered by incorporating two transducers, facilitates a quicker and more efficient inspection regimen. Owing to the long-range propagation ability of the guided wave, it stands out as especially advantageous for larger structures such as solar panels and ship hulls.
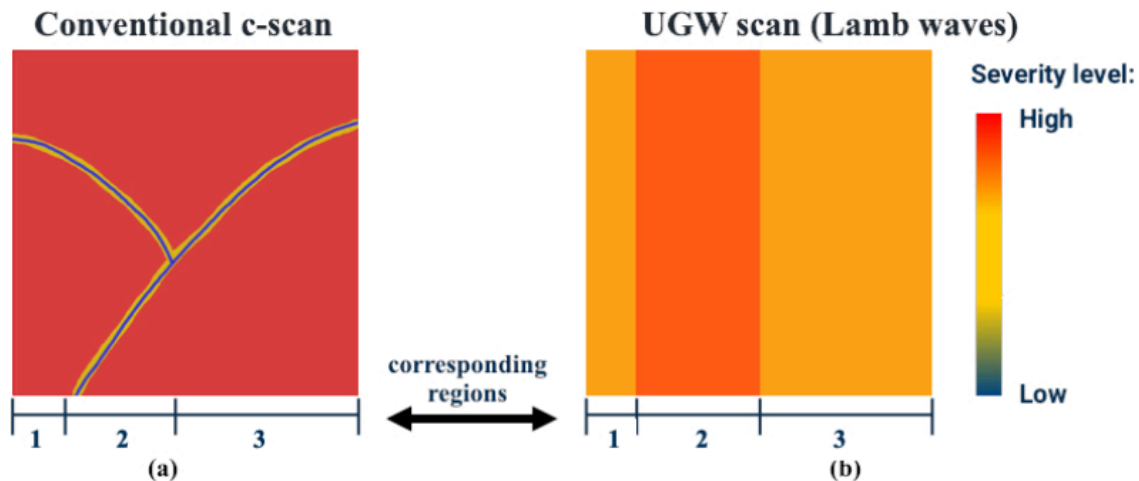


Figure 38: The expected results of (a) conventional C-scan and (b) Lamb waves scan

For instance, **Figure 38** provides a visual comparison of the results obtained from both traditional c-scan and Lamb waves scans. The conventional scan is adept at depicting the precise shape of a crack, while the ultrasonic guided wave (UGW) scan may not delineate the crack's shape. Nevertheless, in the contexts of both solar panels and expansive metal structures, the primary requirement is the identification of a defect's presence rather than its exact shape. The traditional scan mandates a meticulous, point-by-point examination across the plate, whereas the UGW scan rapidly delivers the classification results. A salient benefit of employing Lamb waves as guided waves for non-destructive testing (NDT) is their ability to traverse extensive distances. This stands in contrast to the conventional C-scan method, which relies on bulk waves to inspect the immediate section facing the transducer. With its long-range detection capability, the Lamb waves approach facilitates a more efficient measurement process. If a defect is detected, a more detailed examination can be concentrated on the specific area of interest.

Lamb waves are characterized by their dual propagation modes, symmetric and antisymmetric [24]. These modes propagate within a solid structure and emerge as a result of the interplay between wave behavior and the geometry of the plate they traverse. Symmetric modes produce uniform displacements on both sides of a plate's central plane, while antisymmetric modes yield opposing displacements. As these waves navigate the plate, multiple instances of these modes can coexist, each modulated by parameters like plate thickness and operational frequency.

Dispersion curves delineate the correlation between frequency (or wavelength) and phase velocity for specific wave modes. In the context of Lamb waves and guided waves propagating within a plate, this relationship is multifaceted and exhibits dispersion. This signifies that various frequency components of

the wave traverse at distinct velocities. The dispersion characteristics of Lamb waves are articulated by the Rayleigh-Lamb equations, presented as **Equation 1** (4.1) and (4.2) in the subsequent section.

Equation 1: The dispersion characteristics of Lamb waves

$$\frac{\tan(qd)}{\tan(pd)} = -\frac{4k^2pq}{(q^2 - k^2)^2} \quad \text{for symmetric modes} \tag{4.1}$$

$$\frac{\tan(qd)}{\tan(pd)} = \frac{(q^2 - k^2)^2}{4k^2pq} \quad \text{for antisymmetric modes} \tag{4.2}$$

These equations distinguish between the symmetric and antisymmetric wave propagation modes within a plate. Through numerical solutions of these equations, dispersion curves can be constructed. Such curves offer invaluable insights into the phase velocities associated with various modes across diverse frequencies. For example, there may be instances where the velocity remains consistent across a frequency spectrum, indicating a non-dispersive behavior for that particular mode. Dispersion curves can either be derived experimentally or generated through numerical simulations. The resultant data serves as a foundational tool to comprehend wave behaviors in specific materials or architectural constructs. With the context discussed, the dispersion curves for solar PV modules were subsequently investigated with numerical and experimental outcomes to enhance the understanding of Lamb wave propagation within the material.
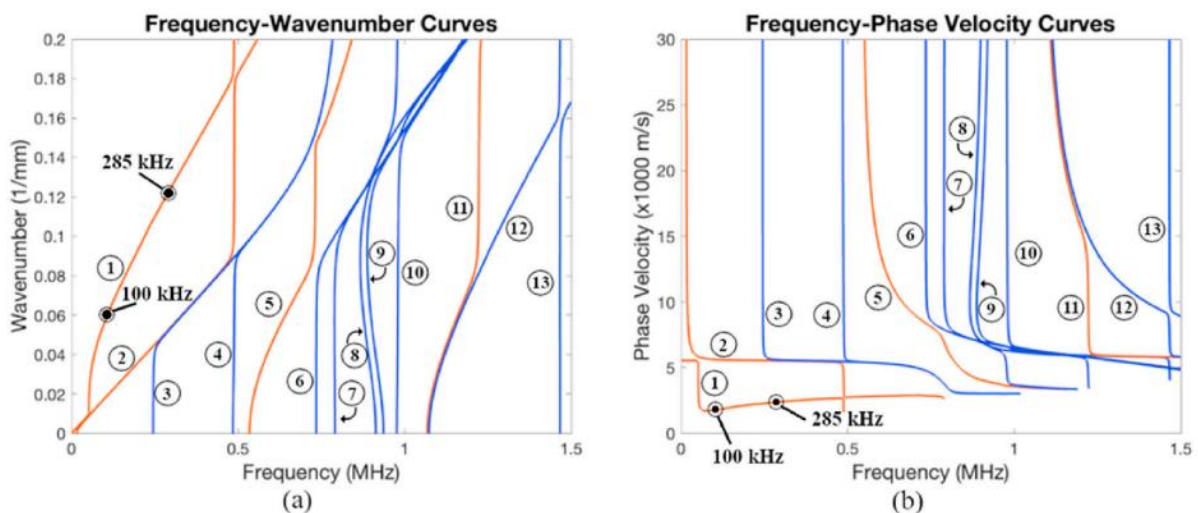


Figure 39: Numerical simulation results: (a) f-k curves,(b) f-vph curves

**Figure 39** presents the results of a numerical simulation using a multilayered plate model to discern the theoretical behavior of ultrasonic-guided waves. This simulation identified 13 potential Lamb modes within a frequency range extending to 1.5 MHz. These modes are depicted in frequency-wavenumber (f-k) and frequency-phase velocity (f-vph) diagrams. Intriguingly, due to the complexities in the plate's structure, some modes exhibit inconsistent symmetry across their spectrum. To illustrate, Mode 1 is symmetric at 100 kHz but becomes antisymmetric at 285 kHz.

Consequently, the conventional labels of symmetric (S) and antisymmetric (A) are employed to denote these modes. In Lamb wave inspection techniques, a prevalent tactic involves activating a mode within its

non-dispersive frequency range. For instance, Mode 2 demonstrates a stable velocity over a broad frequency range, marking it as a prime selection for this methodology. However, while these non-dispersive modes can be easily activated, their extended wavelengths may overlook minute defects. As a result, there might be a need to employ modes more sensitive to defects. More than simply selecting these modes is required; meticulous analysis is paramount to identify them accurately. Furthermore, it is essential to note that Lamb modes transform their shape across their spectrum, transitioning between symmetric and antisymmetric states depending on the frequency.
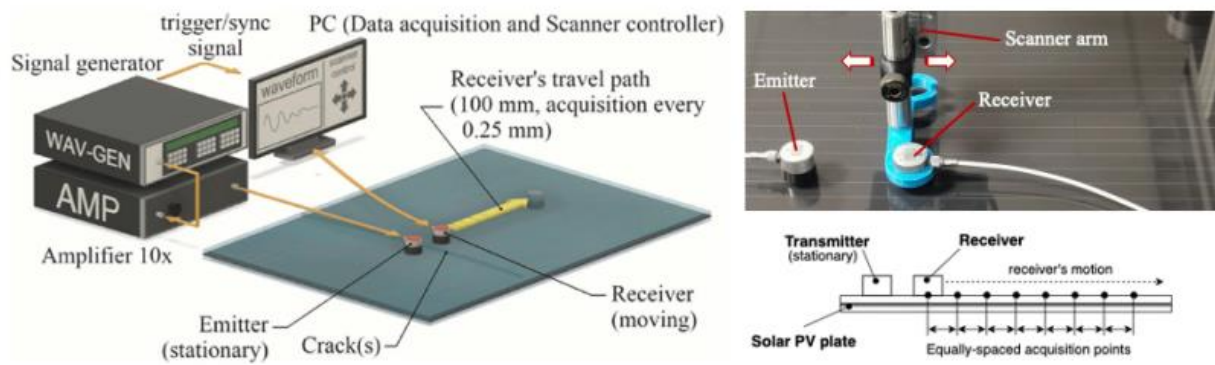


Figure 40: Schematics of the experiments for obtaining Lamb Waves Dispersion Curves

The dispersion curve can also be derived experimentally. **Figure 40** illustrates the experimental setup employed for this purpose. The setup incorporates a pitch-catch arrangement utilizing two contact transducers. One of the transducers acts as an emitter and generates sinusoidal pulses. The second transducer captures the waveforms while traversing a 100 mm path. Both transducers interact with the plate at a perpendicular angle, utilizing water as a couplant to ensure proper contact. This experimental design effectively emulates the conditions of the previous numerical simulation.
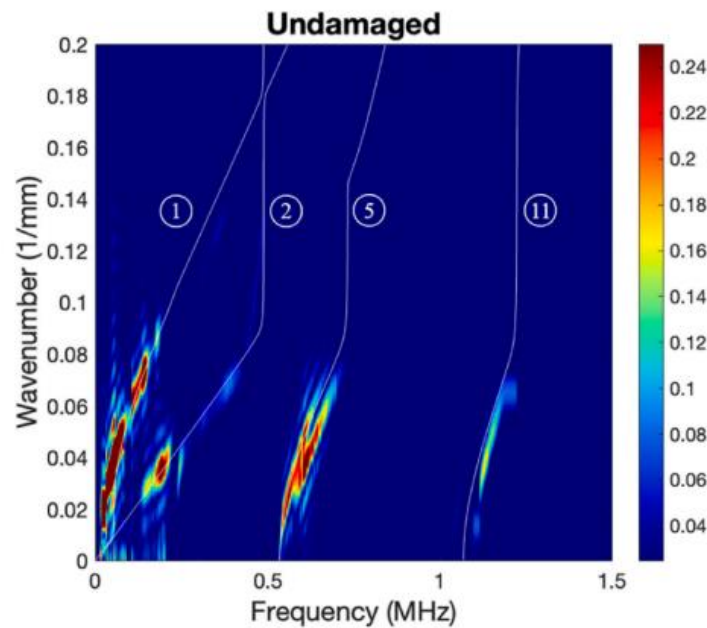


Figure 41: Dispersion curves of Lamb waves in the undamaged area

**Figure 41** presents the data obtained from an undamaged section, which closely aligns with the curves from the numerical simulation. A notable distinction, however, is that in the experimental results, only four

modes are evident, as opposed to the 13 modes observed in the numerical simulation. This discrepancy arises because Lamb wave modes appear with varying intensities based on the specific conditions of the experiment.
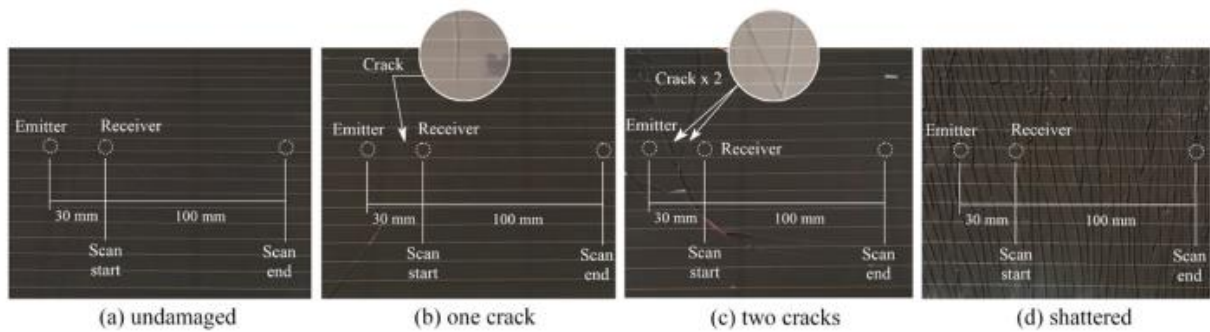


Figure 42: Four sample areas for investigation of Lamb waves - defect interactions

Measurements were performed on four distinct sections, each showcasing different degrees of damage, as illustrated in **Figure 42**. In each experiment, the transducers were initially positioned 30 mm apart. The receiver then moved up to 100 mm from the emitter, capturing data at intervals of 0.25 mm. The selected test spots contained a specific number of cracks within the initial 30 mm separation. The sole exception was the section with shattered glass, where the number of cracks multiplied as the receiver advanced.
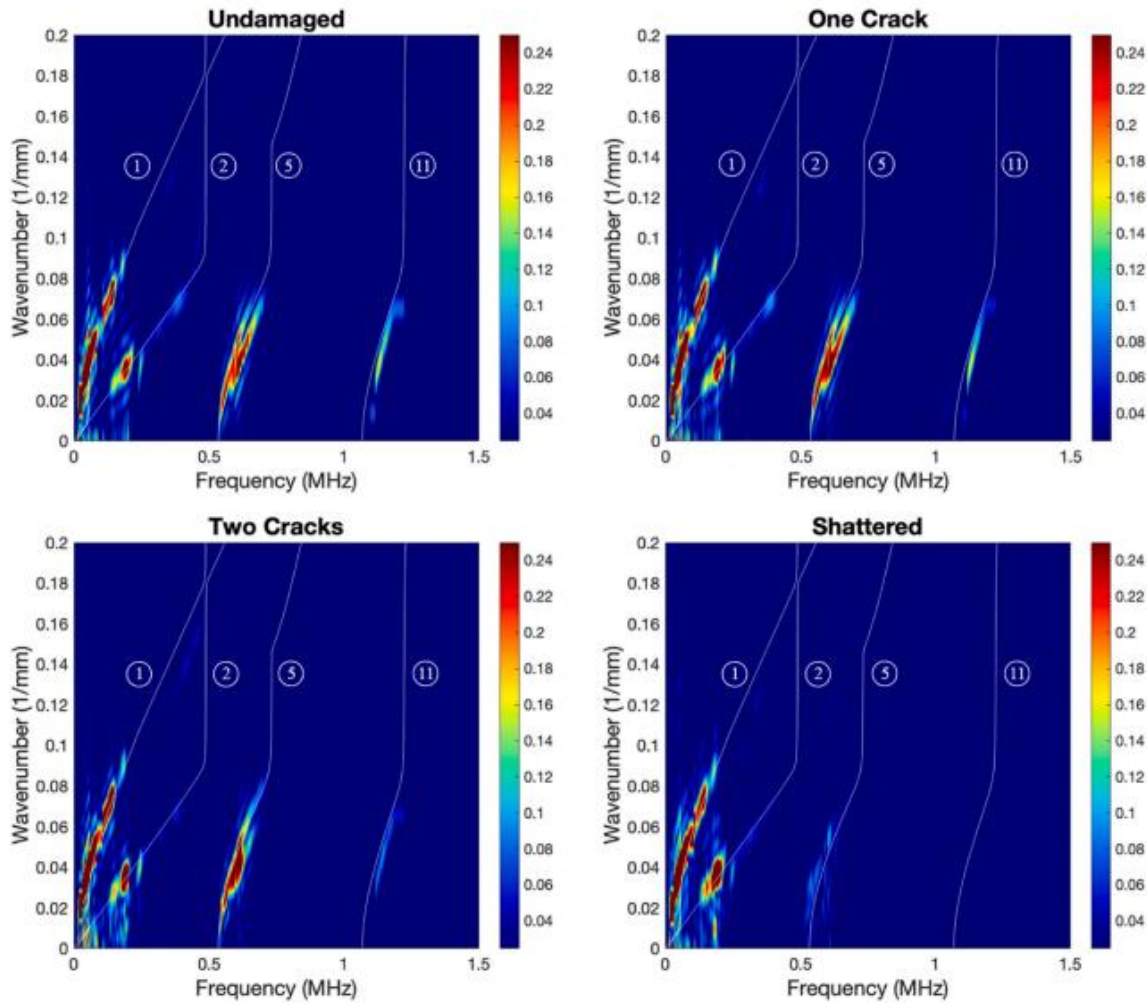
Figure 43: Dispersion curves obtained from areas with different crack severity

**Figure 43** presents four dispersion curve images, each corresponding to areas with different levels of damage, produced using the 2DFFT method. While Modes 1 and 2 remain relatively consistent across all the showcased damage levels, suggesting that they are largely unaffected by the presence of cracks, Modes 5 and 11 exhibit a marked decrease in intensity with increasing damage. Notably, Mode 11's visibility reduces with the number of cracks and disappears entirely in the sample with the shattered glass. Although there is a resemblance between the undamaged and one-crack areas, a meticulous observation reveals a subtle decline in Mode 11's intensity in the latter.



Figure 44: Relative intensity of each mode

A quantitative assessment was done by employing mean pixel intensities from the brighter areas of the images to amplify these findings. It provides a granular perspective on the intensity fluctuations of the various modes a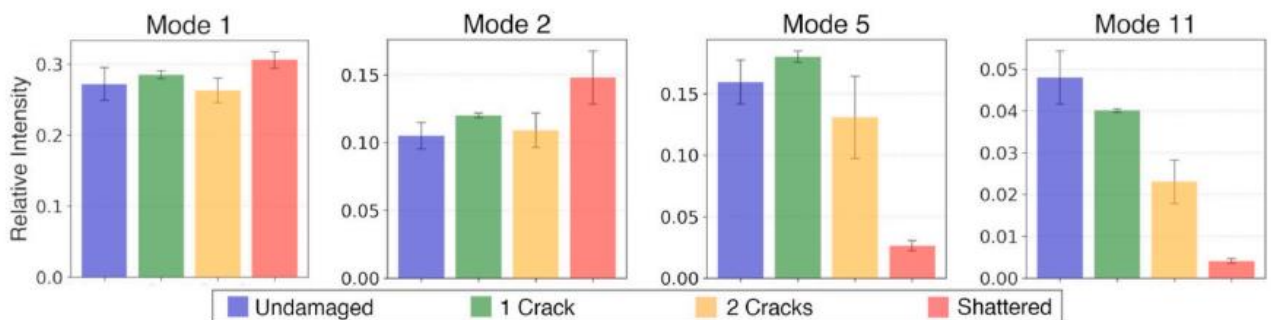cross different damage extents. The bar charts in **Figure 44** depict mode intensities corresponding to various damage scenarios. While the intensity of Modes 1 and 2 remains relatively constant, that of Mode 11 exhibits a sharp decline as crack severity escalates, pointing to its heightened sensitivity to damage. This insight suggests that the intensity variation of Mode 11 could be instrumental in differentiating among the varying degrees of cracks.
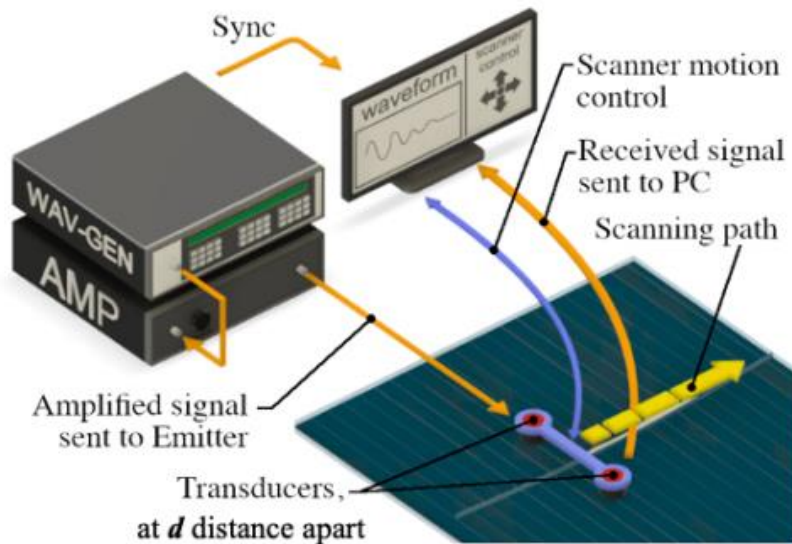


Figure 45: Schematic of Lamb waves scanning with two transducers

Additional measurements were carried out on other sections of the solar panel to delve deeper into the potential damage indicators. The extended experimental configuration, as illustrated in **Figure 45**, employs the pitch-catch technique using two transducers. These transducers, anchored at a predetermined distance on a holder, traverse the solar panel to detect potential cracks. As they journey across the specimen, they analyze the varying regions that fall between them. Subsequent comparisons of these measurements are made to discern indicators of defects.



Figure 46: Measured sections for extracting damage indicators

**Figure 46** illustrates the sections chosen for the experiment. Section A represents a defect-free surface. Section B displays defects throughout the measured part. Section C exhibits a crossing crack spanning from 36mm to 65mm, with the remainder of the section being defect-free.
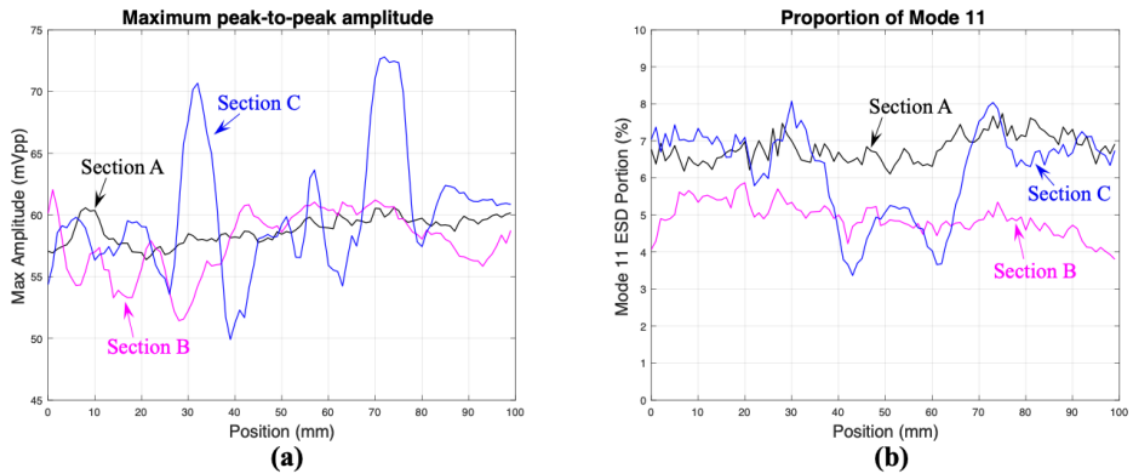
Figure 47: Amplitude of time signal and proportion of Mode 11

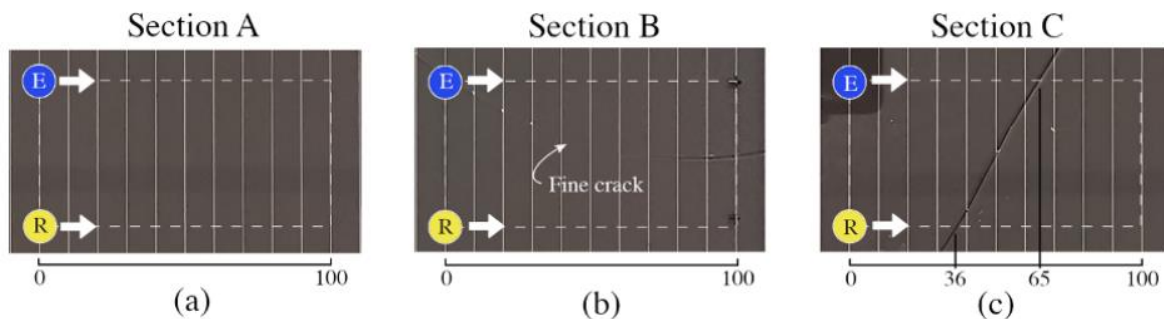Figure 47(a) depicts the ESD ratio of Mode 11, derived from data obtained by scanning the three sections A, B, and C described before. This ESD ratio, expressed as a percentage, signifies the contribution of Mode 11 to the received signal's spectrum. A comparison of the plots in Figure 47(b) reveals that the percentage level for the damaged section is invariably lower than that of the undamaged sections at every scanning point. Notably, a drop in the Mode 11 ESD percentage below 6% signifies the presence of a crack. This method proves adept at detecting even minute, barely discernible cracks, surpassing the accuracy of manual visual inspections.
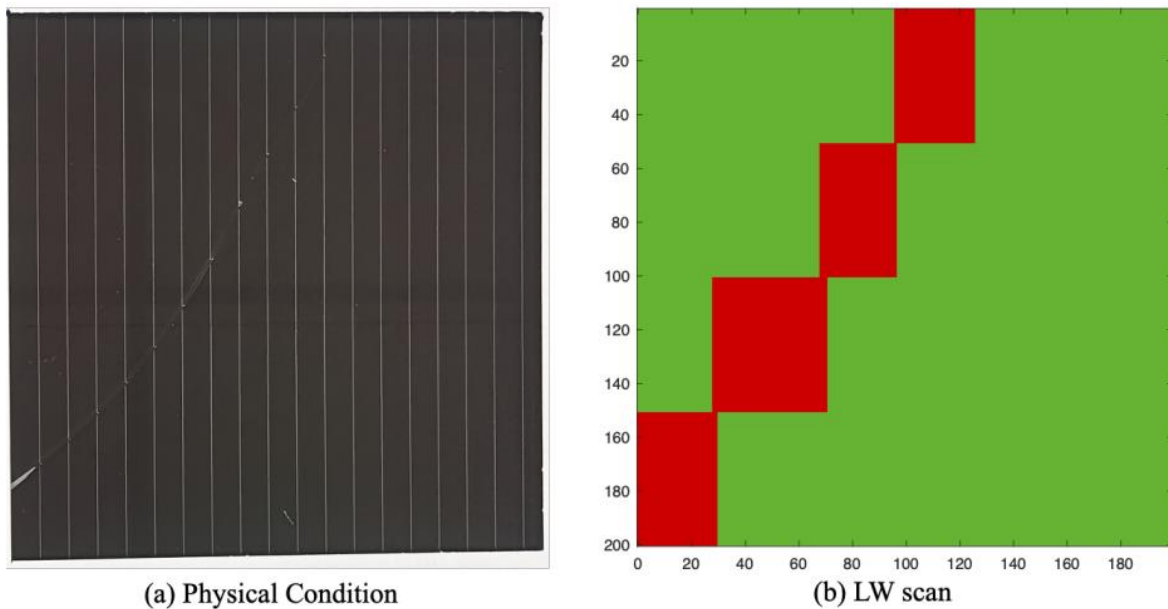


Figure 48: Inspection of crack with the developed Lamb Wave scanning method

The derived damage indicator was applied to Lamb wave scanning in an area with cracks. **Figure 48**(a) visualizes the inspected 200mm × 200mm area, highlighting the crack within. Detection pivoted on the Mode 11 ESD percentage; a value below 6% flagged the presence of a crack. Consequently, the results were binary: green denoted undamaged sections, while red denoted those with cracks, as seen in **Figure 48**(b).

The outcomes adeptly separated the cracked regions, underscoring the efficacy of the Lamb wave method in discerning cracks without delving into specifics about their size or direction. This research paves the way for long-range defect identification in a plate by probing the propagation traits of Lamb waves and each mode's intensity. Leveraging these findings, we anticipate distinguishing defected and non-defected areas by integrating machine learning techniques with the waveforms secured between the emitter and receiver.

## 4.2.    Machine Learning approaches for defect classification

In this subsection, we explore the potential of employing machine learning techniques for the classification of defects. Initially, we utilized a dataset with features selected based on domain expertise. As a preparatory step before delving into metal plates and to ensure our approach was grounded in practical insight, we experimented with solar panel data with the domain knowledge we gathered and discussed in the previous subsection.



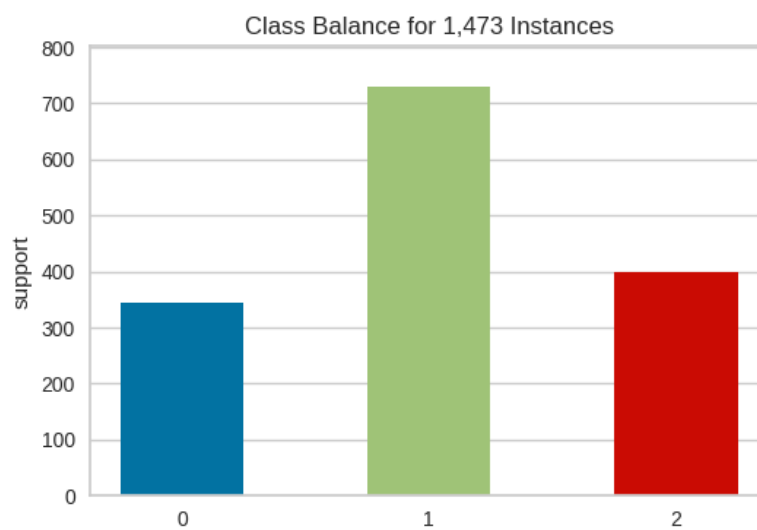Figure 49: Class balance of the dataset

To illustrate the initial conditions of our dataset, **Figure 49** illustrates the class balance within the dataset: class 0 indicates no defect, class 1 signifies the presence of a single crack, and class 2 encompasses multiple cracks, including shattered glass. While class 1 accounts for the most instances, it is still less than class 0 and class 2 combined.
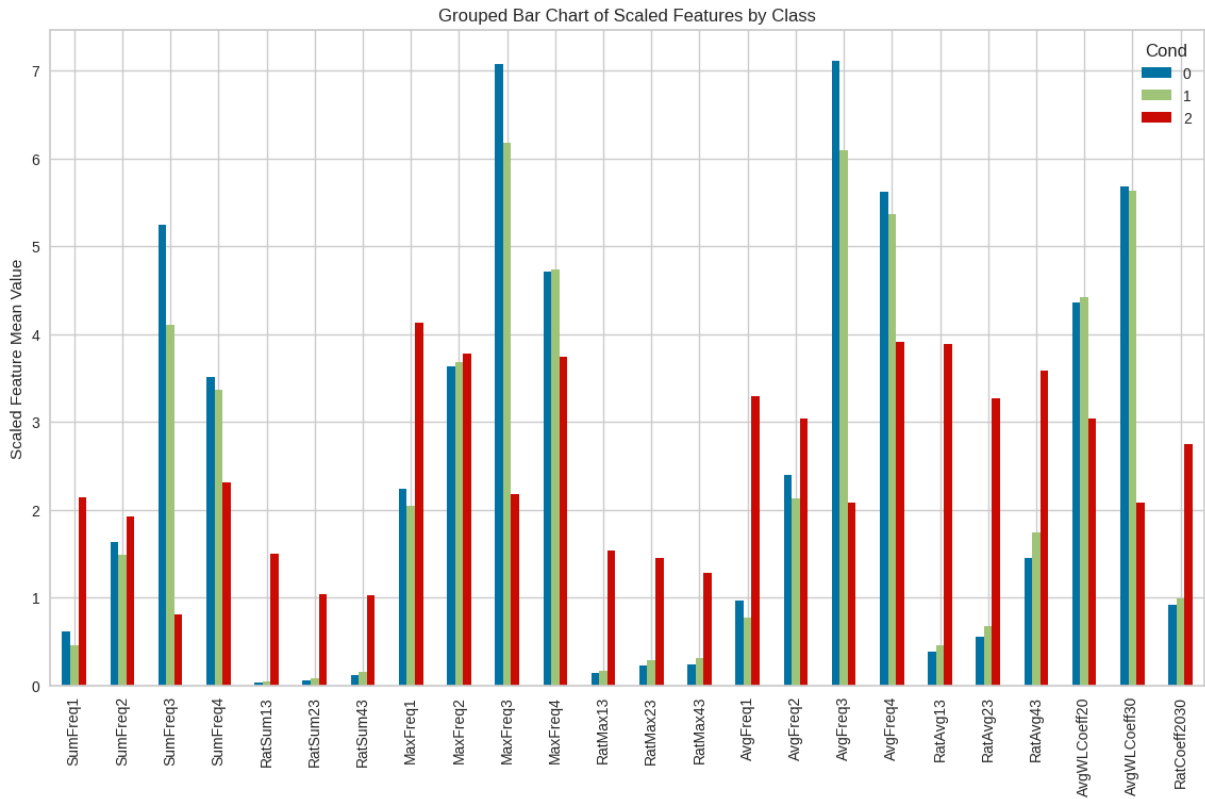
Figure 50: Feature mean per class

Following the class balance, **Figure 50** provides a deeper dive into the data by presenting the mean values of features across different classes. These features were derived using the results from the previous subsection and domain knowledge of ultrasonic waves. "Freq1," "Freq2," and "Freq3," represent major frequency peaks identified in the Fast Fourier Transform (FFT) spectrum. The 'Sum' values, such as "SumFreq1," quantify the area under the curve for the specified frequency bands. 'Avg' and 'Max' provide additional descriptors of the peaks within these bands, while 'Rat' supplies ratios between them. For example, "RatMax13" compares the peak points in "Freq3" to those in "Freq1." Notably, this graph reveals significant variations among the features when comparing different classes, with the greatest distinctions appearing in class 2, which denotes multiple cracks. This suggests potential patterns that machine learning algorithms could exploit for classification.
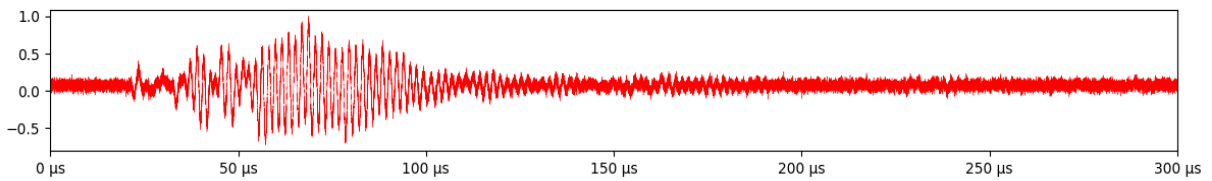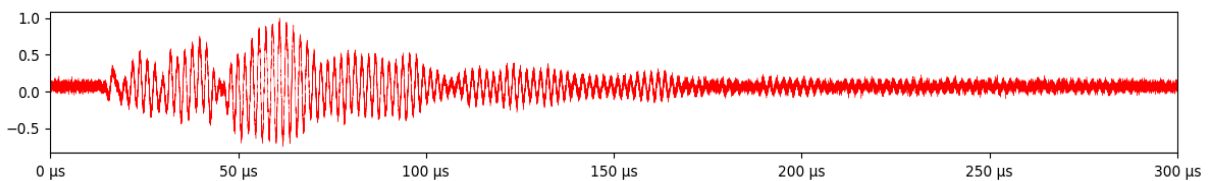


Figure 51: Waveforms of guided waves on solar panel

**Figure 51** provides a visual comparison of the guided waveforms obtained from two different conditions on a solar panel: (a) undamaged and (b) with a crack. Each waveform is the result of precise measurements taken at specific and distinct locations on the solar panel. A number of differences in these two waveforms are observed. However, these two samples were randomly selected, and there are differences due to the presence or absence of cracks, as well as their position in the panel, reflections, etc. This variety underscores the specificity of our data and highlights the necessity of an adaptable model that can discern between subtle differences in structural integrity.



(a) Neural Network  (b) k-nearest neighbors
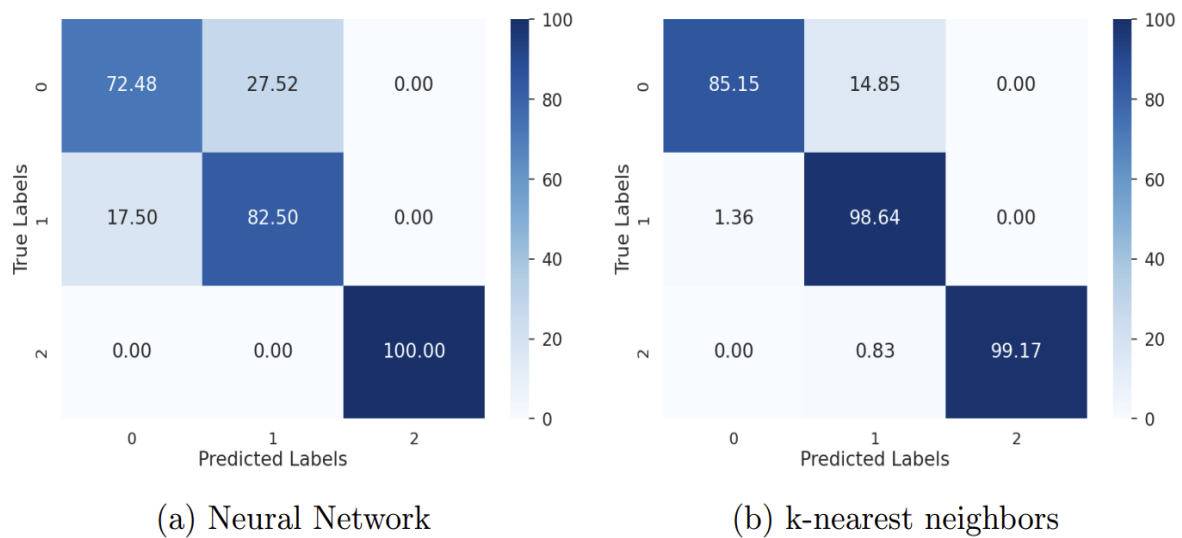
Figure 52: Confusion matrices of (a) Neural Network and (b) k-nearest neighbours

To check the possibility of using machine learning for defect identification, two simple algorithms were applied for the classification, a Neural Network and k-nearest neighbors (k-NN). The confusion matrices in the above **Figure 52**(a) and (b) provide a comparative analysis of the performance of these two classifiers. Using the Neural Network, we achieved a weighted F1 score of 0.85, while the k-NN classifier yielded a superior score of 0.96. It's noteworthy that both classifiers effectively identified class 2, which represents instances of multiple cracks. They exhibited some challenges distinguishing between non-defected panels and those with a single crack, yet they still outperformed a naive classification approach. This result confirmed the feasibility of using machine learning to detect defects in long-range defect detection.

(a) Aluminium Plate
(b) Experimental Setup
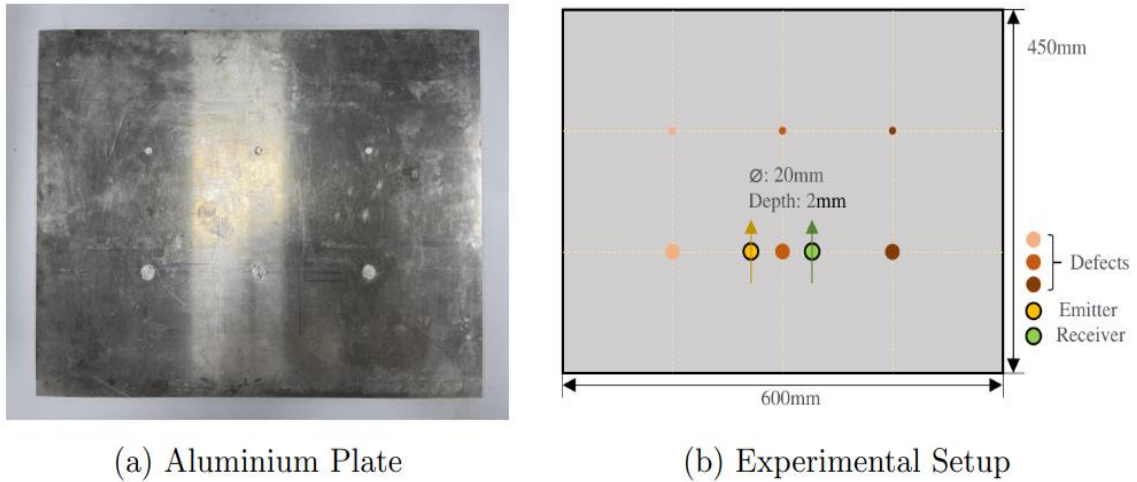
Figure 53: Schematic of Lamb waves scanning with two transducers

**Figure 53** details the experimental setup utilized on an aluminum plate, which measures 6 mm in thickness, 600 mm in width, and 450 mm in height. The plate contains six defects of varying diameters and depths; for the purpose of this experiment, a defect with a diameter of 20 mm and a depth of 2 mm was selected to capture waveforms. Transducers, specifically VS150-M models, served as emitters and receivers to simulate the defects. A DS345 function/ARB generator produced a 300 kHz, 2-burst signal. The emitter and receiver were stationed 60 mm apart, and a series of seven measurements were conducted at 5 mm intervals ranging from -15 mm to +15 mm. At each interval, a waveform was collected at 0.5 mm increments from 0 mm to 60 mm, with the defect located between 20 mm and 40 mm.



Figure 54: Numerical simulation results: dispersion curves of a 6mm aluminium plate

**Figure 54** displays the numerical simulation results for the dispersion curve of a 6 mm thick aluminum plate. Notably, the curve reveals only two modes in the frequency range of 0 MHz to 0.35 MHz. This means that our interpretation has fewer possible modes compare to previous solar panel. The two modes also show a large difference in propagation speed.
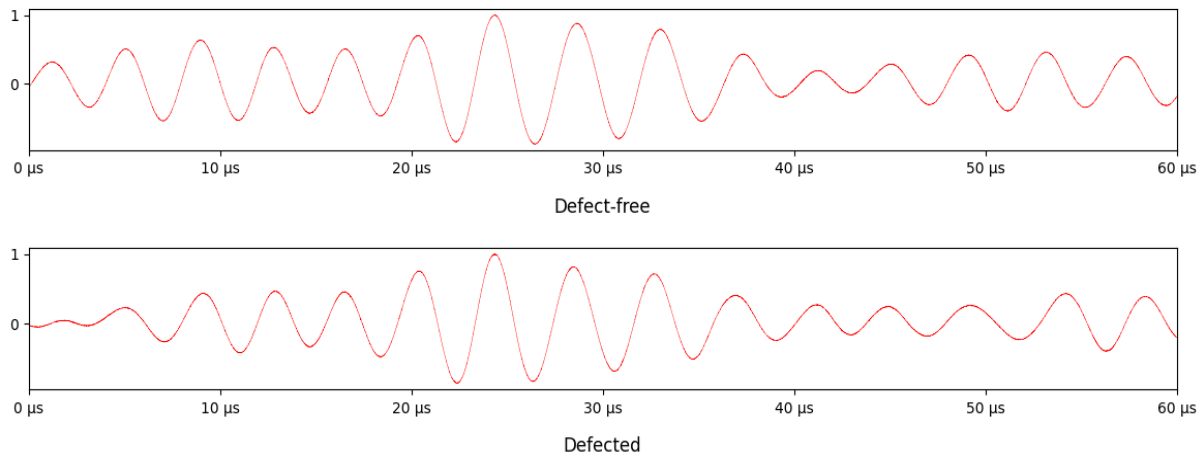


Figure 55: Waveforms of guided waves on aluminium plate
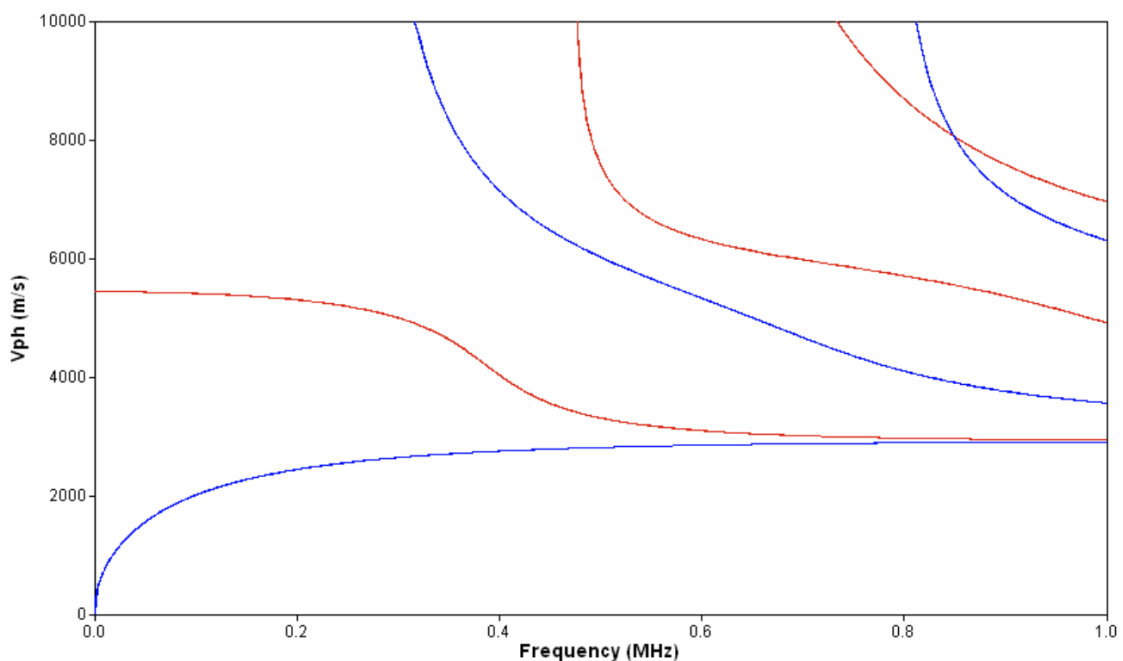
**Figure 55** presents exemplary waveforms obtained from areas on the aluminum plate, both with and without defects. Data collected beyond 60 µs was excluded from subsequent analysis to eliminate the influence of reflections. This decision was informed by the preceding dispersion curve data, which indicated that the slower mode speed exceeds 2000 m/s, translating to a travel time of less than 30 µs for the 60 mm distance between the emitter and receiver. Prior to analysis, each waveform was normalized to reduce the impact of amplitude variations that may result from the use of coupling agents.
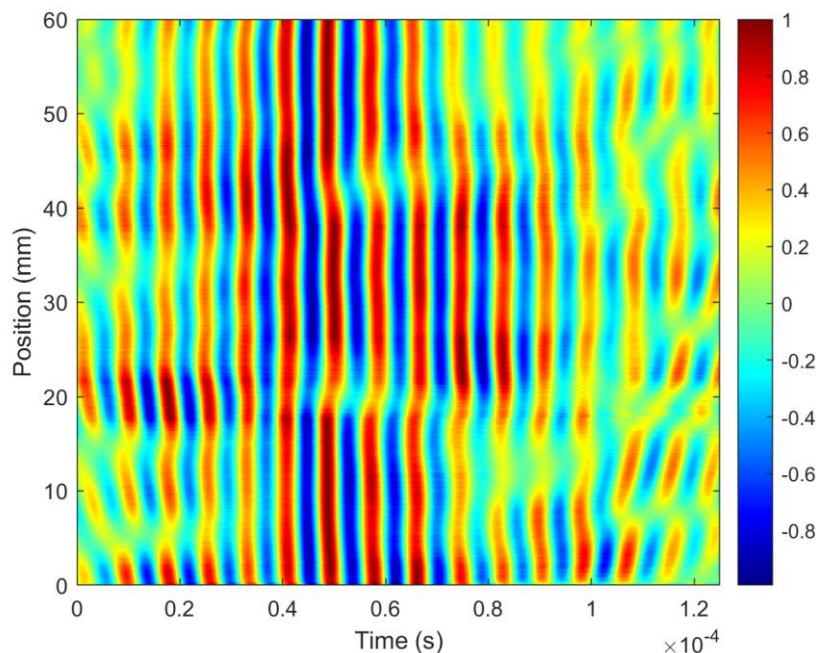


Figure 56: Intensity map of waveform at centre position

**Figure 56** represents an intensity map generated from 120 waveforms measured at the center of an experimental setup. Within the map, the presence of a defect characterized by a depth of 2 mm and a

diameter of 20 mm is notable between 20 mm and 40 mm positions. This defect induces discernible changes in the waveforms when compared to regions without defects. Additionally, waveforms near the boundaries exhibit variations due to phenomena such as reflection.
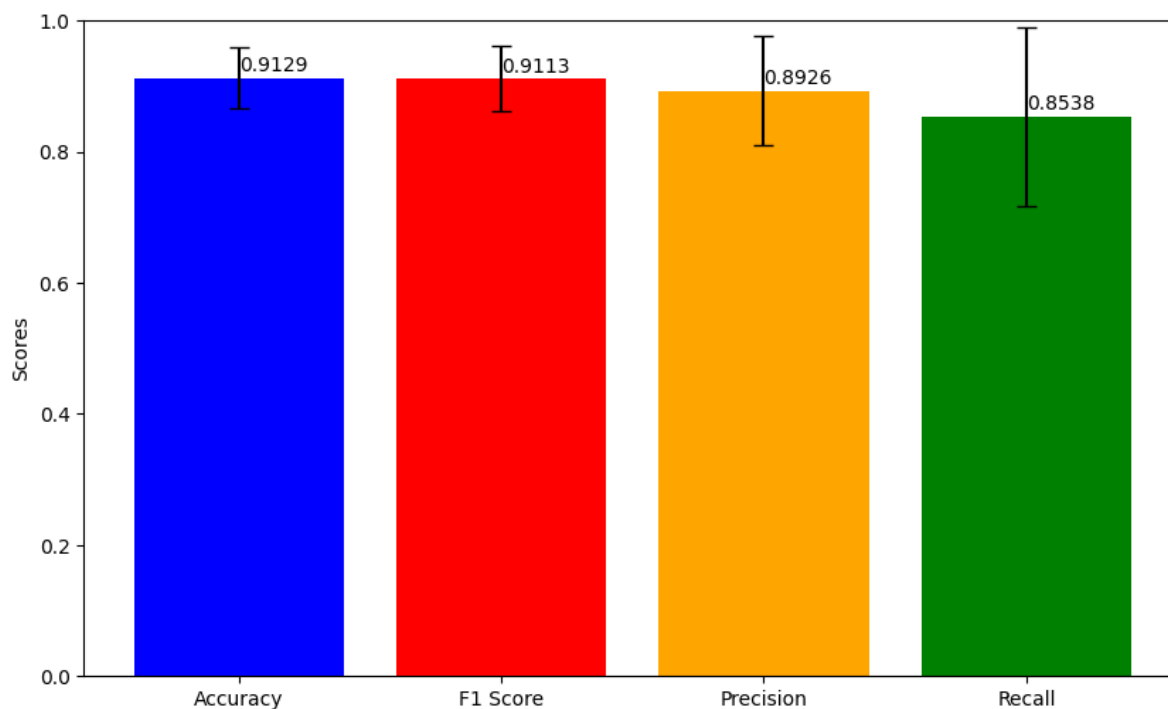


Figure 57: Overall time series classification result

The MINIROCKET algorithm [25], a state-of-the-art method for time series classification, was employed to categorize the collected data. MINIROCKET is renowned for its significant speed advantage over alternative approaches while delivering comparable accuracy. It classifies time series by initially transforming the data through random convolutional kernels, followed by applying a linear classifier to the transformed dataset. For this classification, a dataset comprising 840 measurements gathered from seven distinct locations was used. To prevent data leakage and validate the model's performance, cross-validation was conducted on 21 combinations, allocating five measurements from each location to the training set and two to the testing set.

**Figure 57** presents the outcomes of this classification process. In contrast to a naive classifier's expected accuracy of 0.67, the achieved accuracy of 0.9129, with a standard deviation of 0.047, underscores the algorithm's ability to learn from the provided dataset effectively.

## 4.3.    Defect identification with non-perfect classifier

Section 2 in this deliverable outlined exploration strategies utilizing a perfect detector; however, such an ideal scenario is unlikely in practice. Classifiers typically exhibits some degree of error. This subsection evaluates the ramifications of defect identification when operating with a non-ideal classifier.
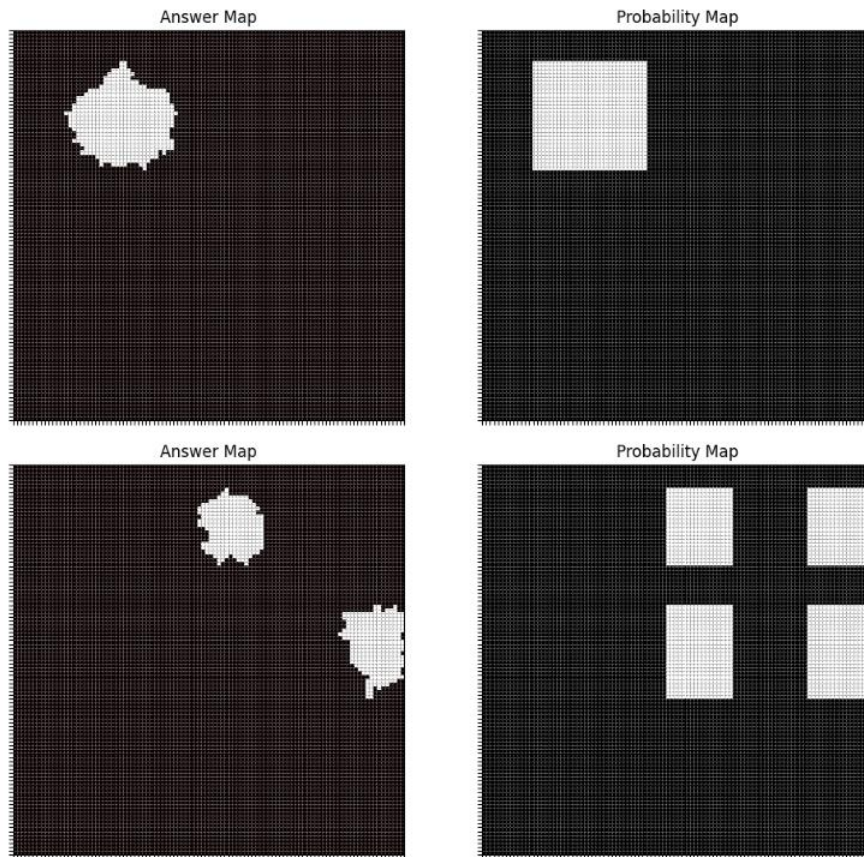
Figure 58: Defect identification simulation with perfect classifier, roller painting

For the simulation, a 100x100 grid was adopted. **Figure 58** illustrates the outcomes when employing the roller painting approach from section 2, presupposing a flawless classifier. A single measurement is conducted per grid square. Similar to Section 2's procedures, a perfect classifier confirms the absence of defects along the line connecting the emitter and receiver if no defect is indicated by the measurement. These results echo those observed in Figure 4, where a solitary defect is represented as a single square independent of the defect's actual shape. When multiple defects are present, each is indicated as a square in the defective area, as well as in adjacent non-defective regions.
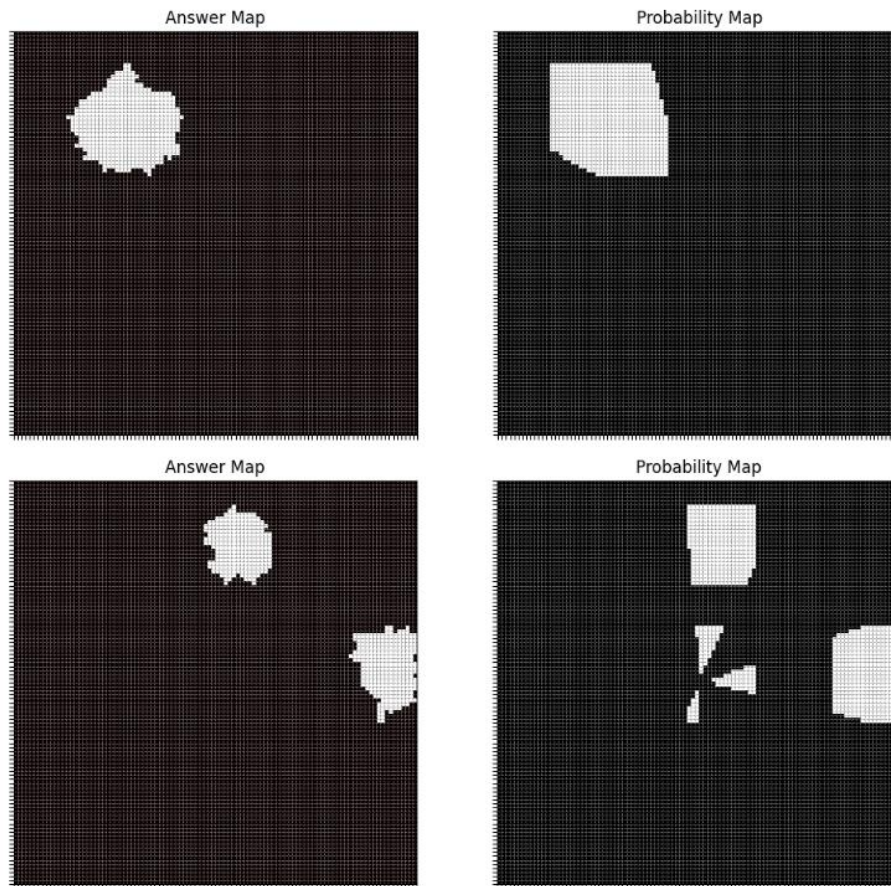
Figure 59: Simulation result with perfect classifier, additional rotation movement

**Figure 59** also presents the simulation outcomes under the presumption of a faultless classifier, with the introduction of a additional rotational movement. Here, both the emitter and receiver execute a single rotation along the corners, originating from a diagonal vertex of the grid. The results show a marginal decrease in the predicted region of defects. While the identification is not entirely accurate, there is a noticeable diminishment in falsely identified defect areas.
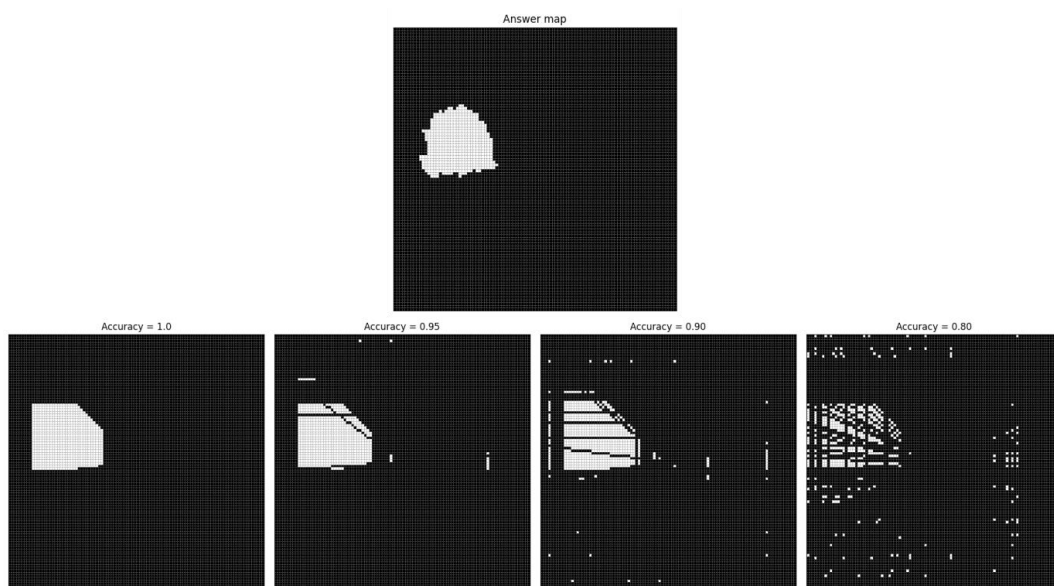


**Figure 60: Simulation result with non-perfect classifier**

Adopting the same movement protocol as in **Figure 59**, but with a non-ideal classifier, Figure 60 displays the resultant simulations. The upper portion of the figure presents the reference answer map, while the lower portion sequentially exhibits the outcomes for classifiers with accuracies of 1.00, 0.95, 0.90, and 0.80, respectively. For each case, precision and recall metrics are maintained at equal levels. At an accuracy of 0.95, a sparse distribution of false negatives appears within the defect zones, coupled with occasional, minuscule false positives in non-defective regions. Decreasing accuracy to 0.90 amplifies the false negatives and introduces small false positives throughout. With an accuracy of 0.80, the simulation highlights a marked escalation in missed actual defects (false negatives) and a pervasive increase in false positives, significantly obfuscating the delineation between defective and non-defective areas.
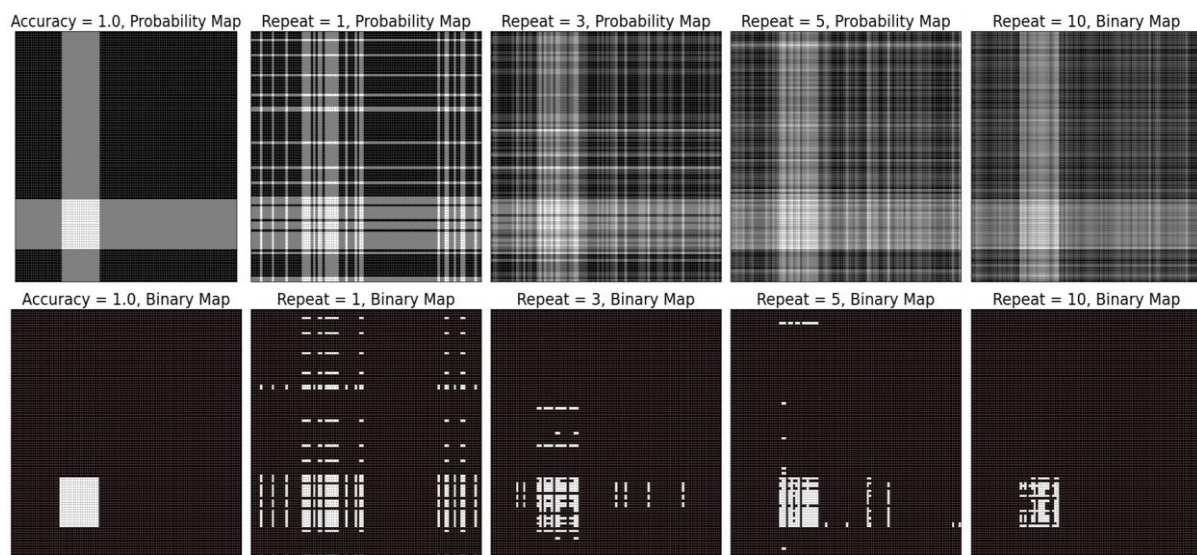


Figure 61: Probability map with non-perfect classifier

For the efficient examination of expansive metal structures, swiftly excluding non-defective zones while reliably detecting and subsequently subjecting actual defects is crucial. Further assessments could be done with methods like C-SCAN. **Figure 61** delineates the simulation results: the upper segment details the probability maps of defects, and the lower segment the derived binary maps with a threshold of 0.75. The far-left display illustrates the ideal scenario with a flawless classifier; the subsequent images model an accuracy of 0.80. "Repeat" denotes the count of measurement iterations per grid cell, with the probability map derived from the quotient of positive defect detections over total measurements. This approach is feasible by setting the grid unit size larger than the measurement interval. Examination of the binary maps reveals a progressive decline in false detections with increasing iterations: initially frequent false positives at a single iteration diminish, so that at ten iterations, defects are predominantly identified within actual defective zones.

## 4.4.    Future work, defect mapping

In this section, we explore the feasibility of extending our methods beyond mere defect detection to include comprehensive defect mapping. To this end, we employ the Radon transform, a technique extensively applied in medical imaging, such as in MRI scans [26].

The Radon transform is an integral transformation that assists in the analysis of two-dimensional images by projecting them at various angles. It functions by summing the pixel values along straight paths,

analogous to the process used in tomographic imaging. In image analysis, the Radon transform proves invaluable for identifying linear features, elucidating image structures, and underpinning computed tomography algorithms.
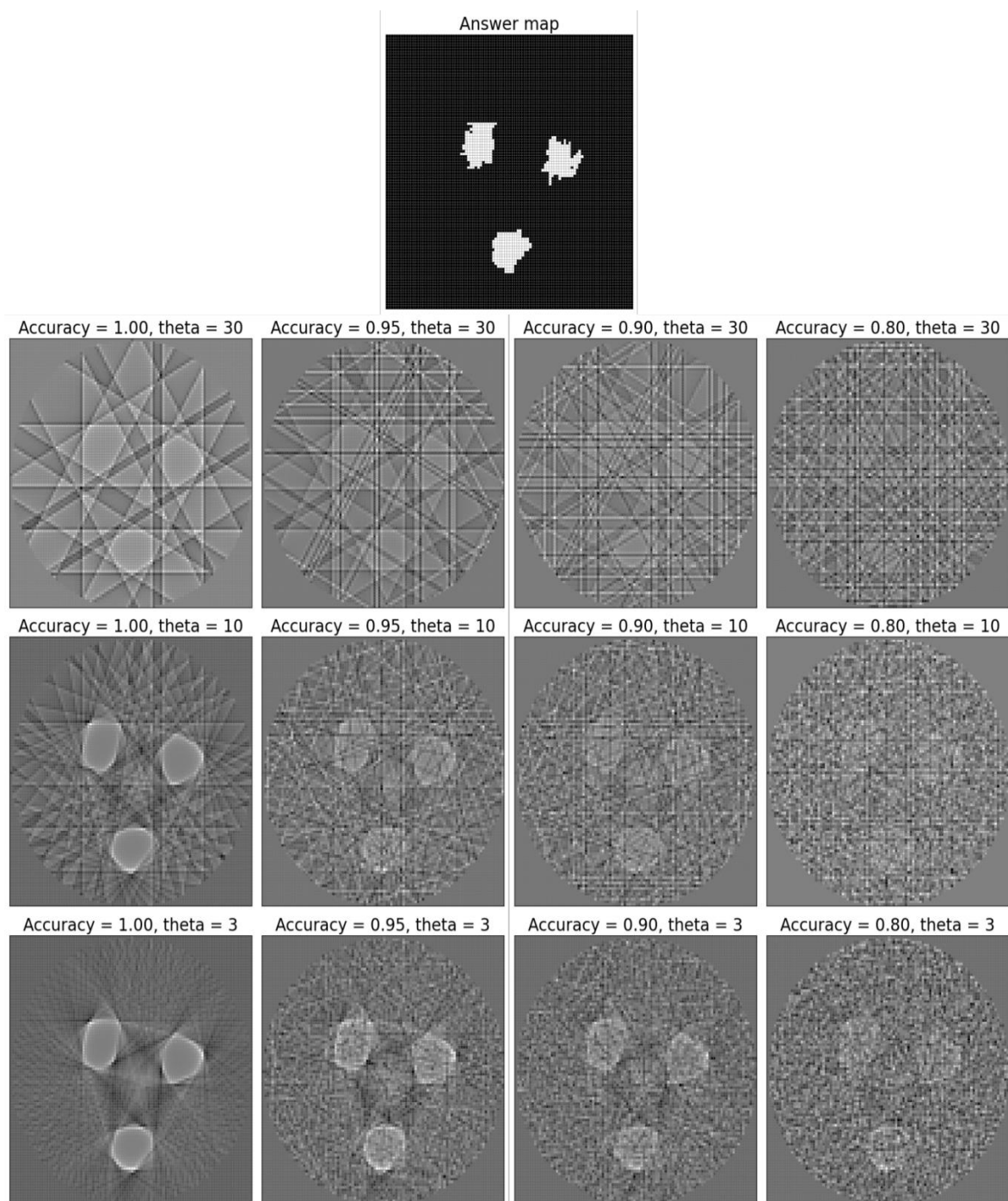


Figure 62: Defect mapping result with radon transform

**Figure 62** graphically conveys the outcomes of the Radon transform when applied to a simulated defect map across different accuracy levels and theta steps. In this context, "theta step" denotes the incremental angular degree used to capture projections at various orientations. The "Answer map" illustrates the initial areas of interest. It is observed that as the accuracy diminishes and theta step alters, the resulting projections become increasingly obscure and distorted, thereby complicating the task of distinguishing the original structures depicted in the "Answer map." Notably, with the theta step reduced from 30 to 3, the

projections offer a more intricate and detailed depiction at higher accuracy levels. The reconstructed images, however, tend to obscure the precise contours of the defects, rendering only an approximate layout. Our objective, nonetheless, is not to delineate the defect's detailed morphology but to localize its presence accurately, which can be refined through subsequent detailed inspections.

An alternative method for achieving precise defect mapping is the Neural Radiance Fields (NeRF) approach. NeRF [27] employs deep learning to represent 3D scenes and the volumetric scene function by processing sparse 2D image sets and training a neural network to predict the color and transparency of light traversing the scene. Its noteworthy capacity to generate detailed 3D reconstructions from limited input renders it a promising candidate for enhanced 2D defect mapping. Utilizing NeRF could potentially allow for more refined and accurate localization of defects.

## 4.5.    Conclusion

In the context of maintaining and inspecting expensive metal structures, the urgency for swift and precise inspection methods is critical. Our research has emphasized the promising capabilities of ultrasonic guided waves, with a particular focus on Lamb waves, for such applications. The wavelets' ability to differentiate between undamaged and defective areas in solar panels has been a testament to this technique's effectiveness. This, coupled with the rapid and broad scanning capabilities of Lamb waves, positions it as a superior alternative for efficient long-range inspections. Incorporation of machine learning techniques further refines this method, offering increased adaptability and precision.

Our investigations into defect classification and identification have yielded insights that attest to the efficacy of the methodologies presented. Machine learning algorithms, notably Neural Networks and k-nearest neighbors, have achieved commendable results in classifying defects in solar panels, with weighted f1 scores of 0.85 and 0.96 respectively. Moreover, the successful application of the advanced time series classification method MINIROCKET for defect identification on an aluminum plate demonstrates the versatility and practicability of these approaches for metal structures.

Nonetheless, machine learning's prowess in defect identification is not without its challenges, particularly when considering the complexities of our target structures. The probability of achieving an ideal or "perfect" classifier is slim, underlining the importance of recognizing the consequences of employing imperfect classifiers. Our simulations reveal that with decreasing classifier accuracy, the incidence of false negatives and positives surges, compromising the integrity of defect localization. Although this could be mitigated by increasing the number of measurements per grid point, it necessitates a trade-off between resolution and inspection duration.

Applying the Radon transform, a mainstay in medical imaging, to defect mapping introduces a pioneering method for visualizing and mapping defects. While it may not capture the minutiae of defects, the Radon transform lays the groundwork for broad-scale defect localization, allowing for more focused detection and leaving detailed scrutiny for subsequent analyses.

In summary, the research has made substantial strides in defect classification and identification on large structures, providing a solid foundation and clear trajectory for future research endeavors. There is a considerable scope for advancement in refining classifier accuracy, mitigating errors from imperfect classification, and improving defect mapping techniques.

# 5.References

**BIBLIOGRAPHIE**

[1]   O.-L. Ouabi, P. Pomarede, N. F. Declercq, N. Zeghidour, M. Geist et C. Pradalier, «Learning the propagation properties of rectangular metal plates for lamb wave- based mapping,» *Ultrasonics,* vol. 123, p. 106 705, 2022.

[2]   P. Huthwaite et F. Simonetti, «High-resolution guided wave tomography,» *Wave Motion,* vol. 50, n° %15, 3, p. 979–99, 2013.

[3]   O.-L. Ouabi, P. Pomarede, M. Geist, N. F. Declercq et C. Pradalier, «A fastslam approach integrating beamforming maps for ultrasound-based robotic inspection of metal structures,» *IEEE Robotics and Automation Letters,* vol. 6, n° %12, p. 2908– 2913, 2021.

[4]   M. Faisal Haider, A. Migot, M. Y. Bhuiyan et V. Giurgiutiu, «Experimental investigation of impact localization in composite plate using newly developed imaging method,» *Inventions,* vol. 3, n° %13, 2018.

[5]   A. Ridani, O.-L. Ouabi, N. F. Declercq et C. Pradalier, «On-plate autonomous ex- ploration for an inspection robot using ultrasonic guided waves,» *2021 European Conference on Mobile Robots (ECMR),* p. 1–6, 2021.

[6]   G. Chahine, P. Schroepfer, O.-L. Ouabi et C. Pradalier, «A magnetic crawler sys- tem for autonomous long-range inspection and maintenance on large structures,» *Sensors,* vol. 22, n° %19, 2022.

[7]   A. Bautin, O. Simonin et F. Charpillet, «MinPos : A Novel Frontier Allocation Algorithm for Multi-robot Exploration,» *ICIRA - 5th International Conference on Intelligent Robotics and Applications,* 2012.

[8]   R. Miorelli, C. FISHER, A. Kulakovskyi, B. CHAPUIS, O. Mesnil et O. d'Almeida, «Defect sizing in guided wave imaging structural health monitoring using convolutional neural networks,» *NDT & E International,* vol. 122, p. 102 480, Jun. 2021.

[9]   M. Couto, C. Souza et P. D. Rezende, «Strategies for optimal placement of surveillance cameras in art galleries,» *GraphiCon 2008 - International Conference on Com- puter Graphics and Vision, Proceedings,* Jan. 2008.

[10]  M. A. Arain, E. Schaffernicht, V. H. Bennetts et A. J. Lilienthal, «The right direction to smell: Efficient sensor planning strategies for robot assisted gas tomography,» *2016 IEEE International Conference on Robotics and Automation (ICRA),* pp. 4275-4281, 2016.

[11]  M. A. Arain, M. Cirillo, V. H. Bennetts, E. Schaffernicht, M. Trincavelli et A. J. Lilienthal, «Efficient measurement planning for remote gas sensing with mobile robots,» *2015 IEEE International Conference on Robotics and Automation (ICRA),* pp. 3428-3434, 2015.

[12] Wikipedia contributors, «Beamforming,» Wikipedia, the free encyclopedia, 2023. [En ligne]. Available: https://en.wikipedia.org/w/index.php?title=Beamforming&oldid=1151960654. [Accès le 15 June 2023].

[13] S. Thrun, M. Montemerlo, D. Koller, B. Wegbreit, J. Nieto et E. Nebot, «Fastslam: An efficient solution to the simultaneous localization and mapping problem with unknown data,» *Journal of Machine Learning Research,* vol. 4, May 2004.

[14] O.-L. Ouabi, A. Ridani, P. Pomarede, N. Zeghidour, N. F. Declercq, M. Geist et C. Pradalier, «Combined Grid and Feature-based Mapping of Metal Structures with Ultrasonic Guides Waves,» *2022 International Conference on Robotics and Automation (ICRA),* pp. 5056-5062, 2022.

[15] Wikipedia contributors, «Piezoelectric sensor,» Wikipedia, the free encyclopedia, , 2023. [En ligne]. Available: https://en.wikipedia.org/w/index.php?title=Piezoelectric sensor&oldid=1154129092. [Accès le 15 June 2023].

[16] Wikipedia Contributors, «Wavelet transform,» Wikipedia, the free encyclopedia, 2023. [En ligne]. Available: https://en.wikipedia. org/w/index.php?title=Wavelet transform&oldid=1147185762. [Accès le 15 June 2023].

[17] Wikipedia Contributors, «Convolutional neural network,» Wikipedia, the free encyclopedia, 2023. [En ligne]. Available: https://en.wikipedia.org/w/index.php?title=Convolutionalneuralnetwork&oldid=1159408824. [Accès le 15 June 2023].

[18] ----, «Shipspotting,» Shipspotting, Mars 2012. [En ligne]. Available: https://www.shipspotting.com/photos/1516924.

[19] H. Song et Y. Yang, «uper-resolution visualization of subwavelength defects via deep learning-enhanced ultrasonic beamforming: A proof-of-principle study,» *NDT & E International,* vol. 116, n° %10963-8695, p. 102344, 2020.

[20] M. Shafiee et M. Abbas, «Structural health monitoring (shm) and determination of surface defects in large metallic structures using ultrasonic guided waves,» *Sensors,* vol. 18, n° %111, p. 3958, 2018.

[21] J. A. Tsanakas, A. van der Heide, T. Radaviˇcius, J. Denafas, E. Lemaire, K. Wang, J. Poortmans et E. Voroshazi, «Towards a circular supply chain for pv modules: Review of today's challenges in pv recycling, refurbishment and re-certification,» *Progress in Photovoltaïcs: Research and Applications,* vol. 28, n° %16, pp. 454-464, 2020.

[22] M. S. Chowdhury, K. S. Rahman, T. Chowdhury, N. Nuthammachot, K. Techato, M. Akhtaruzzaman, S. K. Tiong, K. Sopian et N. Amin, «An overview of solar photovoltaic panels' end-of-life material recycling,» *Energy Strategy Reviews,* vol. 27, p. 100431, 2020.

[23] Z. Su, L. Ye et Y. Lu, «Guided lamb waves for identification of damage in composite structures: A review,» *Journal of sound and vibration,* vol. 295, n° %13-5, p. 753–780, 2006.

[24] I. A. Viktorov, "Rayleigh and lamb waves", New York, NY: Springer, 1967, p. p. 33.

[25] A. Dempster, D. F. Schmidt et G. I. Webb, «MiniRocket: A very fast (almost) deterministic transform for time series classification,» chez *Proceedings of the 27th ACM SIGKDD Conference on Knowledge Discovery and Data Mining.*, New York, 2021.

[26] T. M. Lehmann, C. Gonner et K. Spitzer, «Survey: Interpolation methods in medical image processing,» *IEEE transactions on medical imaging,* vol. 18, n° %111, p. 1049–1075, 1999.

[27] B. Mildenhall, P. P. Srinivasan, M. Tancik, J. T. Barron, R. Ramamoor- thi et R. Ng, «Nerf: Representing scenes as neural radiance fields for view synthesis,» *Communications of the ACM,* vol. 65, n° %11, p. 99–106, 2021.